J. Fluid Mech. (2024), *vol*. 986, A17, doi:10.1017/jfm.2024.317

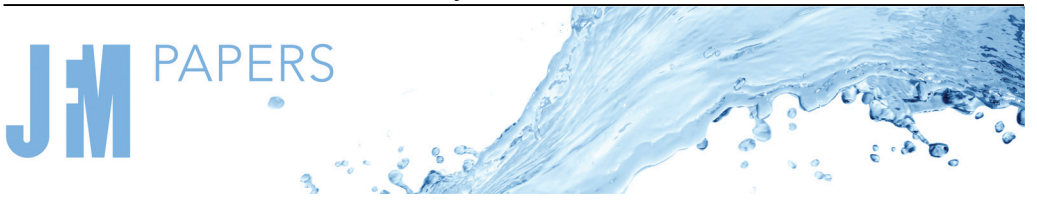

Contact-angle hysteresis on rough surfaces: mechanical energy balance framework

Dalton J.E. Harvie†

Department of Chemical Engineering, University of Melbourne, Parkville, VIC 3010, Australia

(Received 14 December 2023; revised 14 February 2024; accepted 22 March 2024)

Using as a starting point conservation of momentum, a multiphase mechanical energy balance equation is derived that accounts for multiple material phases and interfaces present within a moving control volume. This balance is applied to a control volume that is anchored to a three-phase contact line as it advances continuously over the surface of a rough and chemically homogeneous and inert solid. Using semi-quantitative models for the material behaviour occurring within the control volume, an order of magnitude analysis is performed to neglect insignificant terms, producing an equation for predicting contact-angle hysteresis from a knowledge of the interface dynamics occurring around the three-phase contact line. It is shown that the viscous energy dissipation that occurs during the 'stick–slip' motion of the three-phase contact line, being the cause of contact-angle hysteresis on rough surfaces, can be calculated from changes in intermediate equilibrium interface states. The balance is applied to the Wenzel, Cassie–Baxter and Fakir (super-hydrophobic) wetting states, showing for the Fakir case that significant dissipation occurs during both interface advance and recede, and relating these dissipations to interfacial area changes that occur around the 'stick–slip' events.

Key words: contact lines, wetting and wicking

1. Introduction

The ability of a liquid to 'wet' a solid is described by the angle that the liquid makes with the solid when the interface is stationary – the static contact angle. For a liquid in contact with a smooth and chemically homogeneous and inert surface, this angle θ_e is unique and given by Young's equation. Real surfaces, which are often rough on a variety of length scales, are chemically heterogeneous and/or involve some type of irreversible work of adhesion, display a range of equilibrium contact angles: the maximum is the static

† Email address for correspondence: daltonh@unimelb.edu.au

advancing angle θ_a, above which the interface will advance, and the minimum is the static receding angle θ_r, below which it will recede. The difference between these two angles is defined as the range of contact-angle hysteresis (CAH). The CAH, θ_a and θ_r are critical wetting parameters that determine (for example) how easily drops can move over solid surfaces, under what conditions liquid films will smoothly coat surfaces, or whether gas injection will aid particle floatation. Technologies that depend on CAH angles include established processes such as industrial separation devices or the wetting behaviour of fabrics, through to more novel processes such as transparent self-cleaning surfaces for solar power generation or low-energy liquid fuel separation membranes (Cassie & Baxter 1944; Wu *et al.* 2002; Feng *et al.* 2004; Callies & Quéré 2005; Sun *et al.* 2005; Li *et al.* 2013). For the design and optimisation of these processes, general and validated wetting theories are needed that can predict the CAH range. However, as highlighted via several recent works, such theories are not yet available, with fundamental questions remaining about the nature of the wetting process (Eral, 't Mannetje & Oh 2013; Jiang *et al.* 2019; Erbil 2021; Butt *et al.* 2022). The purpose of this study is to derive an energy conservation framework that can be applied to predict CAH angles.

The early energy-based wetting theories of Wenzel and Cassie remain influential in interpreting wetting phenomena. Considering the energy change that occurs as a liquid/gas interface advances a small distance over the surface of a rough solid, Wenzel (1936) proposed that the apparent contact angle is related to the roughness r of the surface, defined as the total to projected surface area ratio (see § 4.1). In deriving this theory, Wenzel assumed that the liquid completely wets each surface undulation. Cassie & Baxter (1944) recognised that such 'complete' wetting did not necessarily occur, and derived an expression for the apparent contact angle on a partially wet surface in terms of the wetted and non-wetted liquid areas per projected solid area, being f_1 and f_2, respectively (see § 4.1). The Wenzel and Cassie & Baxter equations are useful for understanding and interpreting experimental data; however, theories based solely on these concepts (e.g. Bico, Thiele & Quéré 2002; Patankar 2003) are not predictive as the proportion of solid surface wetted by a liquid is not known *a priori*. Also, these theories give only one static contact angle for a rough structured surface, rather than the CAH range that is observed experimentally.

Another series of works is based on the thermodynamic concept of energy minimisation of an entire drop sitting on a rough surface. Johnson & Dettre (1964) computed the free energy of drops residing at the centre of concentric sinusoidal roughness rings, showing that the energy of the system oscillated as the drop volume increased and the interface advanced over each ring. They interpreted the amplitude of these energy oscillations as energy barriers that must be overcome by macroscopic vibrational energy to allow interface movement, implying that as the height of surface roughness decreases, the range of CAH should also decrease. This conclusion is contrary to experimental evidence, however, which shows that roughness-induced CAH depends strongly on surface topology (relative shape) rather than absolute roughness size, provided that gravitational and Laplace pressure effects can be neglected on the length scale of the roughness (Öner & McCarthy 2000; Dorrer & Rühe 2008; Li *et al.* 2016; Jiang *et al.* 2019). Other studies have used similar static free-energy minimisation concepts to explain CAH for a variety of periodically shaped surfaces (Extrand 2002; Brandon *et al.* 2003; Marmur 2006, 2022); however, in general, the results do not qualitatively agree with observation. For example, Brandon *et al.* (2003) used minimal surface energy modelling to show that the apparent contact-angle range for a drop on a doubly periodic undulating surface approached a single value (the Cassie angle) as the drop size to roughness ratio increased, again contradicting

the above referenced experimental observations that show that the CAH range becomes quite constant at large droplet to roughness size ratios. A related question also remains about these analyses: is it really necessary to consider the energy of the entire flow system (most commonly a droplet) to calculate the CAH range, or is it instead a property associated with the three-phase contact line (TPCL) that can be applied to a wide variety of surrounding flow systems? This is an unresolved question that has garnered conflicting opinions (Extrand 2003; Gao & McCarthy 2007*a*,*b*; McHale 2007; Nosonovsky 2007; Panchagnula & Vedantam 2007; Marmur 2022).

Other studies conclude that CAH is substantially a property of the TPCL region (Nosonovsky 2007; Panchagnula & Vedantam 2007) and that CAH has its origin in the energy dissipation that occurs around the TPCL as it advances over the rough solid. Central to this concept is that the advancing and receding angles are defined as those measured while the interface is moving (albeit at a vanishingly slow velocity) rather than being determined solely by static thermodynamic states. An influential study in this vein is by Joanny & de Gennes (1984), who proposed a model for CAH on a surface that contains a dilute number of 'strong defects' as a model for surface contamination or dilutely distributed surface roughness. The theory considered the 'pinning' and subsequent 'depinning' or 'jumping' of the contact line as it advanced over a surface, assuming that during each interface jump surface potential energy is dissipated to heat. Joanny & de Gennes (1984) calculated this energy dissipation amount under ideal conditions and incorporated it into an equation for CAH relevant to dilute defect surfaces. More recent works have observed experimentally the pinning/depinning or 'stick–slip' behaviour of the fluid interface near the TPCL (Priest *et al.* 2009; Forsberg *et al.* 2010; Schellenberger *et al.* 2016; Jiang *et al.* 2019). Other studies have used a variety of energy conservation principles to extend the work of Joanny & de Gennes (1984) to periodic surfaces (Raj *et al.* 2012; Butt *et al.* 2017; Jiang *et al.* 2019) or interpreted measurements of CAH in terms of contact-line energy dissipation and interfacial 'jumping' dynamics (Priest, Sedev & Ralston 2007, 2013; Dorrer & Rühe 2008; Song *et al.* 2022). Despite these successes, however, questions remain about this conceptual model of CAH; around what specific TPCL region should energy be conserved, how should the dissipation that occurs during the 'stick–slip' motion of the interface be calculated, and how can the energies of practical surfaces that may contain randomly shaped structures and/or micro-bubbles/droplets be included in such an analysis?

On a slightly different track, Joanny & de Gennes (1984) also explored the influence of 'weak' surface defects on CAH, referring to smooth defects as those that cause the fluid interface near the solid to become distorted, but that do not result in the aforementioned 'pinning' and 'depinning' behaviour of the TPCL. Their conclusion was that isolated weak defects do not generally result in hysteresis; however, other works have extended this analysis to conclude that distributions of weak surface heterogeneities can cause CAH (Pomeau & Vannimenus 1985; Robbins & Joanny 1987; Öpik 2000). In related work, Cox (1983) examined how an interface changes as it moves over a gently undulating sinusoidal periodic rough surface, showing that when the interface moved in the direction of roughness periodicity, TPCL 'jumps' occurred (i.e. 'strong' defects leading to CAH), but when advancing in other directions relative to the periodicity direction, the interface moved continuously (i.e. 'weak' defects producing no CAH). It should be noted that these theoretical studies predict the possible shapes that a fluid interface can take when passing over arrangements of surface heterogeneities, and from these, the range of CAH angles is inferred. In general, the link between CAH angles calculated via these interface topology methods and those calculated by energy conservation has not been established.

In reviewing this body of literature, key questions about wetting behaviour remain. Specifically, there is conjecture regarding how energy conservation, fluid interface distortion and the dynamics of interface 'jumping' determine CAH. Critically, there is no experimental consensus or fundamental analysis that shows how energy conservation should be applied to predict CAH – works that are based on energy conservation around entire droplets in general do not predict experimentally observed CAH trends, while studies that are based on energy changes around a moving TPCL lack rigour, leading to inconsistent formulations and application. Further, while many studies do view contact-line jumping as a source of CAH ('strong' defects), there is confusion over whether fluid interface distortion ('weak' defects) in isolation can produce CAH, and how studies that predict CAH angles via interface topology and dynamics can be mathematically related to CAH angles resulting from energy conservation.

This study addresses these questions. Specifically, we derive a rigorous energy conservation framework, which, when applied to the moving TPCL, can be used to predict CAH. We do this by first deriving a general multiphase mechanical energy balance (MMEB) equation (§ 2) that adds terms associated with the interfacial stresses acting between each of the material phases to the conventional single phase mechanical energy balance. We then apply this MMEB to a cylindrical control volume that is anchored to a TPCL as it moves across a rough solid surface at a vanishingly slow speed (§ 3), deriving an energy conservation equation that predicts CAH from knowledge of the interfacial dynamics occurring within the TPCL. Within § 4, we discuss under what physical conditions the theory is valid, apply the theory to the common Wenzel, Cassie–Baxter and 'Fakir' wetting regimes, and finally outline how the theory answers some of the open questions in the wetting field.

2. Macroscopic mechanical energy balance for immiscible multiphase mixtures

In this section, a macroscopic mechanical energy balance is derived for a moving control volume that contains a number of immiscible phases (see figure 1). The derivation is similar to that of Bird, Stewart & Lightfoot (2002, p. 221, § 7.8) except that interfacial tension acts at the interface between each pair of phases, and the balance is not specific to Newtonian liquids. (We do assume that each material has a symmetric stress tensor; however, for most homogeneous materials, this assumption appears to be valid (Kuiken 1995; Dahler & Scriven 1961).)

The starting point is a momentum equation for a mixture of immiscible phases,

$$\frac{\partial}{\partial t}\rho \boldsymbol{v} + \boldsymbol{\nabla}\cdot\rho\boldsymbol{v}\boldsymbol{v} = \boldsymbol{\nabla}\cdot[T_M + T_S] + \rho\boldsymbol{g}. \tag{2.1}$$

Here, $\boldsymbol{v}$ is the local phase velocity (assumed to vary continuously throughout), ρ is the local phase density, T_M is the local total material stress at any point within any phase, and T_S is the local surface stress acting on the interfaces between phases. The functional form of the material stress tensor $T_M(\boldsymbol{x})$ is a property of the material type present at $\boldsymbol{x}$.

Formally, for (2.1) to be valid everywhere within V_{cv}, all terms appearing in the equation must be defined not only within each phase but also on the interfaces between phases. This includes terms such as T_M and ρ that are associated with a particular material type. Such formal definitions could be made; however, as (2.1) is integrated over space in the following analysis, as long as any phase-specific terms are finite on each interface, their interface values do not affect the final energy balance. Hence we simply assume that the interface values for $T_M(\boldsymbol{x})$ and ρ are finite.

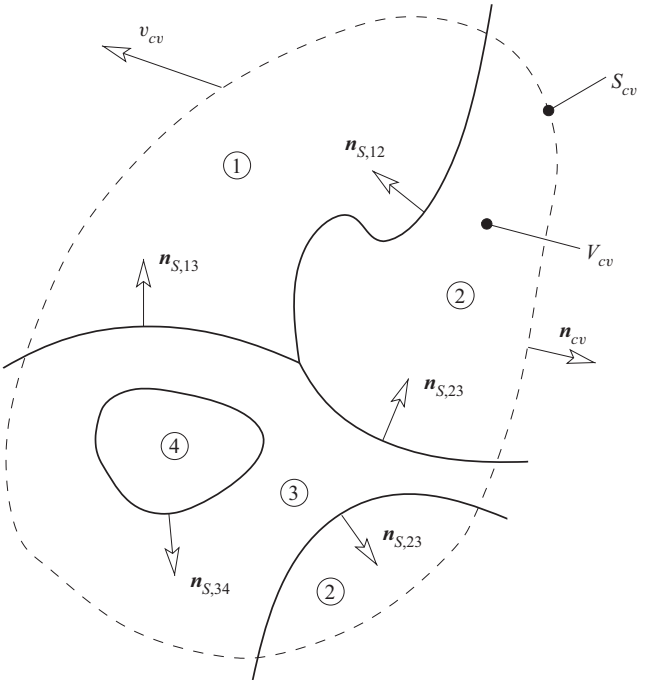

Figure 1. The macroscopic mechanical energy balance is performed on a moving control volume that contains multiple immiscible phases bounded by multiple interface types. Each interface type has an associated unit normal vector $\boldsymbol{n}_{S,ij}$ that is directed into phase i (where $i < j$). The velocity and outward unit normal of the control volume boundary are $\boldsymbol{v}_{cv}$ and $\boldsymbol{n}_{cv}$, respectively. In the indicated configuration, four material phases are present within the control volume, and they intersect along four different interface types.

The effects of interfacial tension on material movement are captured using a surface stress tensor $\boldsymbol{T}_S(\boldsymbol{x})$. The form of this tensor is taken from Lafaurie *et al.* (1994), but generalised here to include interfaces between multiple phases:

$$\boldsymbol{T}_S(\boldsymbol{x}) = \sum_{i<j} \sigma_{ij}(\boldsymbol{I} - \boldsymbol{n}_{S,ij}\boldsymbol{n}_{S,ij})\,\delta_{S,ij}. \tag{2.2}$$

In this equation, σ_{ij} is the constant surface energy per unit area (or interfacial tension) associated with the 'ij interface' (i.e. the interface between phases i and j), $\boldsymbol{I}$ is the identity tensor, $\boldsymbol{n}_{S,ij}$ is a unit vector directed normal to the ij interface and into phase i, and $\delta_{S,ij}$ is a 'surface' delta function that is non-zero only on the ij interface. The surface delta function is essentially a multidimensional analogue of the Dirac delta function and has been utilised extensively in the development of computational fluid dynamics methods (Brackbill, Kothe & Zemach 1992; Lafaurie *et al.* 1994). In the present context, it has the property that

$$\int_{V_{cv}} \delta_{S,ij}\,\mathrm{d}V = A_{ij}, \tag{2.3}$$

where A_{ij} is the total area of the ij interface existing within the control volume V_{cv}. Further, under conditions where $\boldsymbol{n}_{cv} \cdot \boldsymbol{n}_{S,ij}$ is uniform over a particular intersection between a surface S_{cv} and an interface defined by $\delta_{S,ij}$, the surface integral of the surface delta

function is given by

$$\int_{S_{cv}} \delta_{S,ij}\,\mathrm{d}S = \frac{l_{ij}}{\sqrt{1-(\boldsymbol{n}_{cv}\cdot\boldsymbol{n}_{S,ij})^2}}, \tag{2.4}$$

where l_{ij} represents the line length of the intersection between the two surfaces, and $\boldsymbol{n}_{cv}$ is a unit normal to the surface S_{cv}. These properties of the surface delta function and others are discussed in more detail in Appendix A.

Note that in general, interfacial stresses will act at each one of the immiscible material boundaries that exist within V_{cv}. Consequently, the sum in (2.2) cycles through all possible phase combinations under the condition that $i<j$; that is, $j=1\rightarrow m$ and $i=1\rightarrow j$, where m is the total number of material phases present. Thus stresses from a possible $(m-1)!$ interface types may be included in the momentum balance.

By using (2.2) to represent surface stresses, three assumptions about the system are implied. First, as the surface stress is a sum of contributions from each interface type, we have neglected any 'line tension' stresses that may occur at the intersection between interfaces. While no consensus regarding the existence of these stresses has been reached in the literature, most studies suggest that even if line tension does exist, it has a negligible effect on macroscopically measurable contact angles (Boruvka & Neumann 1977; Marmur 1997, 2006; Pompe, Fery & Herminghaus 1999). Second, by assuming constant surface energies for each interface type, we have neglected any Marangoni forces that would exist if surfactants or thermal gradients were present within the control volume. Third, the assumption of constant surface energies also implies that the process of surface creation or destruction is reversible on a molecular scale. We discuss implications of this assumption in § 4.4.

With the immiscible multiphase momentum equation defined, we take the dot product of (2.1) with the local velocity $\boldsymbol{v}$ and then integrate the result over the volume V_{cv}. Noting that both the stress tensors T_M and T_S are symmetric, application of the Leibniz formula for differentiating a volume integral, the Gauss–Ostrogradskii theorem and the compressible continuity equation yields

$$\begin{aligned}\frac{\mathrm{d}}{\mathrm{d}t}\int_{V_{cv}}\left(\frac{1}{2}\rho v^2+\rho\hat{\Phi}\right)\mathrm{d}V = &\int_{S_{cv}}\boldsymbol{n}_{cv}\cdot\left[\left(\frac{1}{2}\rho v^2+\rho\hat{\Phi}\right)(\boldsymbol{v}_{cv}-\boldsymbol{v})\right]\mathrm{d}S\\ &+\int_{S_{cv}}\boldsymbol{n}_{cv}\cdot[\mathsf{T}_M\cdot\boldsymbol{v}]\,\mathrm{d}S-\int_{V_{cv}}\mathsf{T}_M:\nabla\boldsymbol{v}\,\mathrm{d}V\\ &+\int_{S_{cv}}\boldsymbol{n}_{cv}\cdot[\mathsf{T}_S\cdot\boldsymbol{v}]\,\mathrm{d}S-\int_{V_{cv}}\mathsf{T}_S:\nabla\boldsymbol{v}\,\mathrm{d}V.\end{aligned} \tag{2.5}$$

Here, $\boldsymbol{v}_{cv}$ and $\boldsymbol{n}_{cv}$ are the velocity and outwardly directed unit normal of the control volume boundary S_{cv}, respectively, v is the magnitude of the local velocity $\boldsymbol{v}$, and $\hat{\Phi}$ is a gravitational potential function satisfying $\boldsymbol{g}=-\nabla\hat{\Phi}$.

To simplify (2.5) further, we concentrate on the last two terms on the right-hand side, which relate to interfacial stresses. For the first of these, we substitute in the surface stress definition of (2.2) to find

$$\int_{S_{cv}}\boldsymbol{n}_{cv}\cdot[\mathsf{T}_S\cdot\boldsymbol{v}]\,\mathrm{d}S=\sum_{i<j}\sigma_{ij}\int_{S_{cv}}\delta_{S,ij}(\boldsymbol{I}-\boldsymbol{n}_{S,ij}\boldsymbol{n}_{S,ij}):\boldsymbol{v}\boldsymbol{n}_{cv}\,\mathrm{d}S. \tag{2.6}$$

For the second term, we use the surface delta function transport equation derived in Appendix A:

$$\frac{\partial \delta_{S,ij}}{\partial t} + \boldsymbol{\nabla} \cdot (\delta_{S,ij} \boldsymbol{v}) = \delta_{S,ij} (\boldsymbol{I} - \boldsymbol{n}_{S,ij} \boldsymbol{n}_{S,ij}) : \boldsymbol{\nabla} \boldsymbol{v}. \tag{2.7}$$

Substituting T_S from (2.2) into the second interfacial stress term of (2.5), and then using the right-hand side of (2.7) to expand the double dot product gives

$$\begin{aligned} \int_{V_{cv}} T_S : \boldsymbol{\nabla} \boldsymbol{v} \, \mathrm{d}V &= \sum_{i<j} \int_{V_{cv}} \sigma_{ij} \delta_{S,ij} (\boldsymbol{I} - \boldsymbol{n}_{\mathrm{S},ij} \boldsymbol{n}_{S,ij}) : \boldsymbol{\nabla} \boldsymbol{v} \, \mathrm{d}V \\ &= \sum_{i<j} \int_{V_{cv}} \frac{\partial (\sigma_{ij} \delta_{S,ij})}{\partial t} + \boldsymbol{\nabla} \cdot (\sigma_{ij} \delta_{S,ij} \boldsymbol{v}) \, \mathrm{d}V. \end{aligned} \tag{2.8}$$

Using the scalar Leibniz theorem on the first term on the right-hand side of this equation and the Gauss–Ostrogradskii theorem on the second term yields

$$\int_{V_{cv}} T_S : \boldsymbol{\nabla} \boldsymbol{v} \, \mathrm{d}V = \sum_{i<j} \left\{ \frac{\mathrm{d}}{\mathrm{d}t} (\sigma_{ij} A_{ij}) - \int_{S_{cv}} \boldsymbol{n}_{cv} \cdot [\sigma_{ij} \delta_{S,ij} (\boldsymbol{v}_{cv} - \boldsymbol{v})] \, \mathrm{d}S \right\}, \tag{2.9}$$

where (2.3) has been used to relate surface area to the volume integral of $\delta_{S,ij}$.

Finally, substituting (2.6) and (2.9) back into (2.5) and simplifying the material stress surface integral gives the immiscible MMEB valid for compressible and incompressible materials:

$$\begin{aligned} &\underbrace{\frac{\mathrm{d}}{\mathrm{d}t} \left[\int_{V_{cv}} \left(\frac{1}{2} \rho v^2 + \rho \hat{\Phi} \right) \mathrm{d}V + \sum_{i<j} \sigma_{ij} A_{ij} \right]}_{\text{rate of change of kinetic, gravitational potential and interfacial surface energy within } V_{cv}} \\ &= \underbrace{\int_{S_{cv}} \boldsymbol{n}_{cv} \cdot \left[\left(\frac{1}{2} \rho v^2 + \rho \hat{\Phi} + \sum_{i<j} \sigma_{ij} \delta_{S,ij} \right) (\boldsymbol{v}_{cv} - \boldsymbol{v}) \right] \mathrm{d}S}_{\text{rate at which kinetic, gravitational potential and interfacial surface energy are advected into } V_{cv}} \\ &+ \underbrace{\sum_{i<j} \sigma_{ij} \int_{S_{cv}} \delta_{S,ij} (\boldsymbol{I} - \boldsymbol{n}_{S,ij} \boldsymbol{n}_{S,ij}) : \boldsymbol{v} \boldsymbol{n}_{cv} \, \mathrm{d}S}_{\text{rate of work done on the contents of } V_{cv} \text{ by interfacial tension acting at } S_{cv}} \\ &+ \underbrace{\int_{S_{cv}} T_M : \boldsymbol{v} \boldsymbol{n}_{cv} \, \mathrm{d}S}_{\substack{\text{rate of work done on the} \\ \text{contents of } V_{cv} \text{ by} \\ \text{material stresses acting} \\ \text{at } S_{cv}}} - \underbrace{\int_{V_{cv}} T_M : \boldsymbol{\nabla} \boldsymbol{v} \, \mathrm{d}V}_{\substack{\text{rate at which energy} \\ \text{dissipates to heat via} \\ \text{material stresses acting} \\ \text{within } V_{cv}}}. \end{aligned} \tag{2.10}$$

Along with the usual terms found in the single-phase mechanical energy balance (Bird *et al.* 2002, p. 81, § 3.3), the MMEB of (2.10) contains three interfacial stress terms: the first

represents the rate of change of interfacial energy contained within the control volume; the second represents the rate at which interfacial energy is advected across the control volume surface; and the third represents the rate at which interfacial stresses perform work on the control volume at the control volume surface.

To the best of our knowledge, this MMEB equation has not been derived previously. James & Lowengrub (2004), based on the work of Batchelor (1967, p. 132), give an equation that is similar but concerns the material derivative of an infinitesimal surface element, rather than the material derivative of the surface delta function. In a different context, Yue (2020, B11, p. 899) provides a mechanical energy conservation equation that includes surface potential energy, but is expressed in terms of phase field variables.

Equation (2.10) should serve as a useful generic tool for examining energy conservation in flowing systems that possess phase interfaces. For example, the equation could also be used to examine the behaviour of foams or emulsions, applied either locally around phase interfaces to look at structure stability, or globally to understand conservation of bubble/droplet collections. Within the remainder of the paper, we apply the MMEB to understand contact-angle behaviour for a liquid interface advancing over a rough solid.

3. Calculating the advancing contact angle on a rough solid surface

Here, we analyse the macroscopic contact angle of an interface between two immiscible fluids that slowly advances over a rough solid. The analysis uses the MMEB derived in § 2, applied to a small control volume (CV) that moves with the advancing TPCL across the surface of the solid. Using semi-quantitative models for material and interface behaviour, an order of magnitude analysis is performed to determine which terms within the energy balance are significant, and from this an expression for the advancing contact angle is found that is valid in the limit of an infinitely slowly moving interface.

3.1. *Defining the physical system and moving CV geometry*

Figure 2 illustrates the physical system. Two fluid phases, labelled ① and ②, are bounded below by a solid phase, labelled Ⓢ. The fluids may be either liquids or gases, but are completely insoluble with each other (immiscible) and with the solid, incompressible, and above a certain length scale h_{mol} (for molecular), act as continua. The implications of these assumptions are discussed further below and in § 4. The surface of the solid is rough, having undulations of a maximum characteristic size h_{rough}. (Two-dimensional roughness topologies such as long ridges or concentric rings are not covered by this theory as these shapes have one dimension that is infinitely long.) A hydrodynamic flow is occurring on a length scale of $h_{surround}$ that is much larger than h_{rough}. This flow slowly drives the fluid interface to the right, hence phase ① is slowly advancing over the solid, while phase ② is slowly receding.

The MMEB of (2.10) is applied to a moving CV as it advances at a constant velocity $\boldsymbol{v}_{cv} = v_{cv}\boldsymbol{e}_1$ over a distance X_{cv} along the solid surface. This is illustrated in figure 2(*b*). Note that v_{cv} is characteristic of the surrounding flow. The CV contains and is approximately centred on the TPCL, defined as the intersection between the advancing fluid interface and rough solid surface. The moving CV has the geometry of a cylinder with radius r_{cv} and length l_{cv}. The dimensions of the volume are smaller than those of the surrounding hydrodynamic flow ($h_{surround}$), yet larger than those of the solid surface roughness (h_{rough}). Hence, noting the above description of the physical system and CV

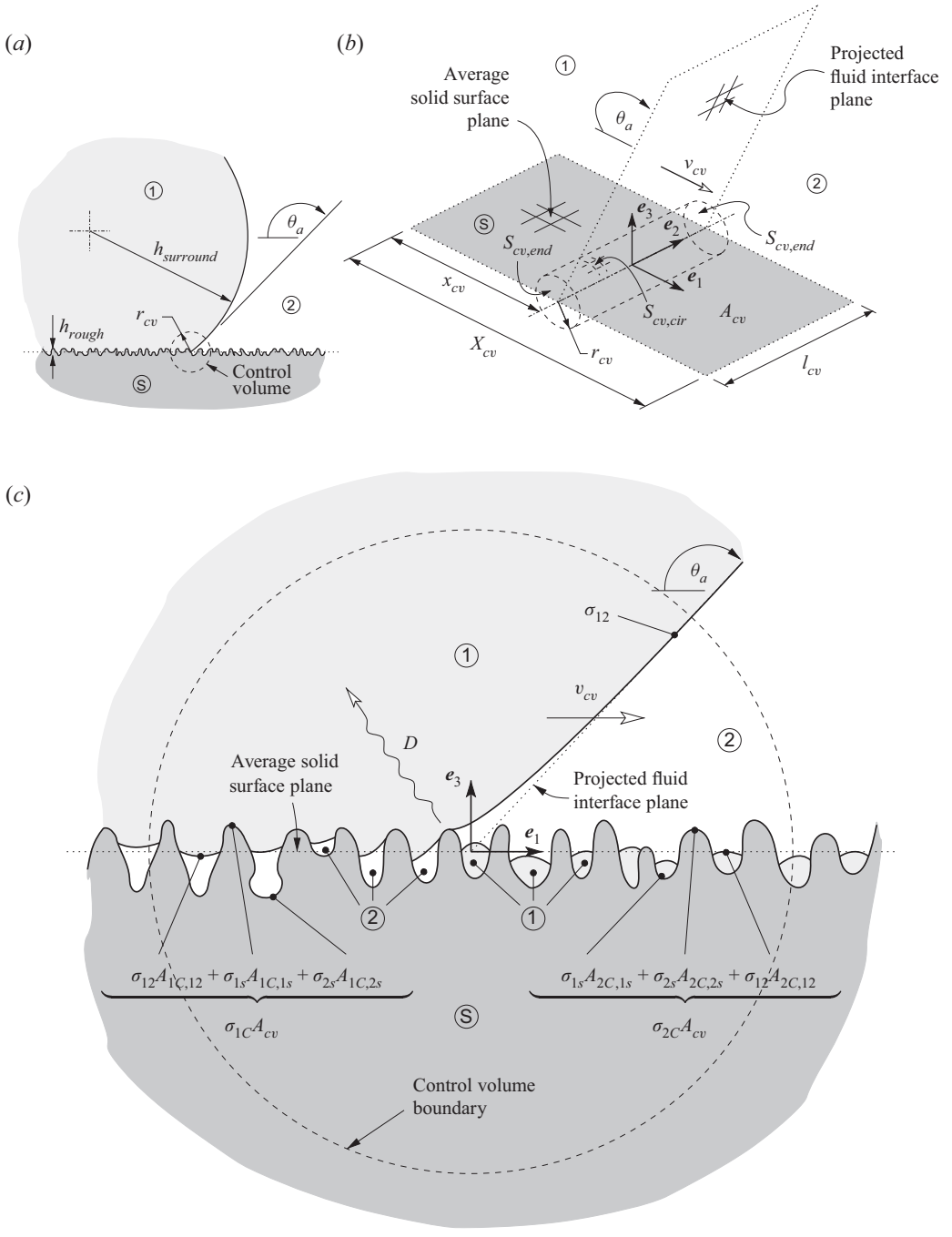

Figure 2. The MMEB is performed over a cylindrical CV that is located at the intersection of the average solid surface and projected fluid interface planes, and moves forward over the solid at a speed of v_{cv} and distance X_{cv}. (*a*,*b*) The region surrounding the CV and contact line on a macroscopic scale. (*c*) The same region on the scale of the CV and solid surface roughness. The symbols ①, ② and Ⓢ indicate regions of phase-1 fluid, phase-2 fluid and solid, respectively.

geometry, we effectively assume the separation of four length scales in our analysis:

$$h_{mol} \ll h_{rough} \ll r_{cv}, l_{cv}, X_{cv} \ll h_{surround}. \tag{3.1}$$

Defining τ as the time taken for the CV to advance the entire distance X_{cv}, it follows that $X_{cv} = v_{cv}\tau$.

The precise centreline of the moving CV is defined to lie at the intersection between two averaged planes: the 'average solid surface plane' and the 'projected fluid interface plane'. The locations of these planes are defined as those of the solid surface and fluid interfaces, respectively, averaged over distances of $O(r_{cv})$ (where $O(z)$ means 'order z'). As the solid surface roughness h_{rough} is of much smaller size than r_{cv}, it follows that the average solid surface plane is perfectly flat on the length scale of the CV. The topology of the fluid interface is governed by the momentum and surface stress equations ((2.1) and (2.2), respectively), combined with boundary conditions specifying how the interface interacts with the solid surface. The specific boundary condition that we employ for the microscopic contact angle is Young's equation, expressed as

$$[\boldsymbol{n}_{S,12}]_{TPCL} \cdot \boldsymbol{n}_w = \cos\theta_e, \tag{3.2}$$

where $[\boldsymbol{n}_{S,12}]_{TPCL}$ is the unit normal to the fluid interface at a point on the TPCL, $\boldsymbol{n}_w$ is the outwardly directed wall normal at the same contact point, and θ_e is the equilibrium or 'Young's' angle. As (3.2) specifies a direct relationship between the fluid interface ($\boldsymbol{n}_{S,12}$) and solid ($\boldsymbol{n}_w$) normals along the TPCL, it follows that close to the rough solid surface, the fluid interface will have local curvatures that are characteristic of the solid roughness – that is, of $O(1/h_{rough})$ – and that these curvatures will exist within distances of $O(h_{rough})$ from the TPCL. Conversely, further from the solid surface, the topology of the interface varies over the larger length scales of the surrounding flow (indeed, this can be used to define $h_{surround}$), so the curvature of the interface there approaches $O(1/h_{surround})$. Hence, as $h_{rough} \ll r_{cv} \ll h_{surround}$ (see (3.1)), averaging the actual fluid interface over $O(r_{cv})$ produces a projected fluid interface plane that is perfectly flat on the length scales of the CV, and as the centreline of the CV is defined as the intersection between the projected fluid interface plane and average solid surface plane, on the scale of the CV, its geometry is that of a perfect cylinder, with a perfectly straight centreline.

This description of the fluid interface topology and relationship to the geometry of the CV has implications when applying the MMEB. At distances of $O(r_{cv})$ from the TPCL, the actual fluid interface and projected fluid interface will at all times be coincident and perfectly flat on these length scales. Hence, given that the projected fluid interface is used to define the centreline of the CV, the actual fluid interface will intersect the circumference of the CV (labelled as $S_{cv,cir}$ in figure 2*b*) in a perfectly normal direction. Similarly, along the ends of the CV (labelled as $S_{cv,end}$ in figure 2*b*) and at distances greater than $O(h_{rough})$ from the TPCL, the actual fluid interface will be flat, coincident with the projected fluid interface, and perfectly normal to the CV boundary. Closer to the TPCL, however, the interface will undulate with curvatures of $O(1/h_{rough})$, crossing the CV boundary at angles that are not necessarily normal to $S_{cv,end}$.

The contact angle of phase ① on the macroscopic length scale is defined as θ. It is the angle between the average solid surface plane and fluid interface plane, measured through phase ①. Equivalently, consistent with the above, it is the angle between the average solid surface plane and actual fluid interface measured at distances of $O(r_{cv})$ from the TPCL. The objective of our analysis is to determine the minimum macroscopic angle that just causes the fluid interface to advance continually over the solid surface, albeit at the vanishingly slow velocity v_{cv}. An equivalent objective is to find the maximum macroscopic

angle that just allows the fluid interface to remain stationary. Either definition represents the advancing angle of phase ① over solid Ⓢ in the presence of phase ② and is referred to as θ_a (for 'advancing'). Formally, $\theta_a = \lim_{v_{cv}\to 0}\theta$.

Note that as phase ① advances over the solid, phase ② recedes. Thus an equivalent objective is to find the receding angle of phase ② ($\theta_{r,2} = \pi - \theta_a$). Indeed, by swapping the physical properties between phases ① and ② (detailed in § 4.1), we can use the same analysis to determine the range of angles over which a fluid interface will remain stationary – that is, the range of CAH.

3.2. *Describing material dynamics within the moving CV*

As well as defining the physical system and CV geometry used in the MMEB, to be able to perform an order of magnitude analysis on its various terms, we need to describe quantitatively how the materials within the volume behave as a function of both space and time. Specifically, we need conceptual models for how the fluid velocities, pressures, interface topology and solid stresses vary as the CV advances.

Within the fluid phase, we assume that for the majority of the advancing time τ, the TPCL and surrounding fluid both move continuously at the slow speeds of $O(v_{cv})$. We refer to the system as being in 'equilibrium' when this is the case, and define the velocity field existing during these times as $\tilde{\boldsymbol{v}} = O(v_{cv})$. However, at certain times during τ, local areas of the TPCL will become pinned by particular surface defects, creating local interface deflections that become larger as the remainder of the TPCL continues to advance. Eventually, once the surrounding TPCL has advanced some distance of $O(h_{rough})$ from the pinning location, these contact-line sections will either detach from the surface defect and return to the main TPCL, or detach from the TPCL and form isolated bubbles/droplets of entrained fluid within the surface roughness. Either way, these detachment processes cause the local TPCL and surrounding fluid to move at much faster capillary-driven speeds than the continuous CV advance speed (v_{cv}), causing a viscous dissipation of energy. This 'stick–slip' dissipative motion has been described previously as one cause of CAH (Joanny & de Gennes 1984; Raj *et al.* 2012; Butt *et al.* 2017; Jiang *et al.* 2019) and as discussed in the Introduction has also been observed experimentally (Priest *et al.* 2009; Forsberg *et al.* 2010; Schellenberger *et al.* 2016; Jiang *et al.* 2019). In this study, we define the local interface and fluid speeds associated with these capillary-driven events as $\hat{\boldsymbol{v}} = O(v_{cap})$, and the total time during which there is a dissipation event occurring within the CV as τ_{cap}. We further assume that the number of defects within the CV (N) is small enough and the capillary velocity (v_{cap}) large enough that only one dissipation event occurs within the CV at any one time. With these assumptions, and for convenience assuming that the analysis duration τ commences and finishes while the system is in equilibrium, we can split the total time over which the analysis is being conducted into a number of 'dissipation events' (N) and 'equilibrium stages' ($N+1$), with the kth dissipation event starting at $\hat{t}_k$ and lasting for $\widehat{\Delta t}_k$, and the kth equilibrium stage starting at $\tilde{t}_k$ and lasting for $\widetilde{\Delta t}_k$. The schematic timeline of figure 3 illustrates this decomposition. The following relationships result:

$$\left.\begin{gathered}\tau_{cap} = \sum_{k=1}^{N}\widehat{\Delta t}_k, \quad \tau = \sum_{k=1}^{N+1}\widetilde{\Delta t}_k + \tau_{cap},\\ \widehat{\Delta t}_k = \tilde{t}_{k+1} - \hat{t}_k, \quad \widetilde{\Delta t}_k = \hat{t}_k - \tilde{t}_k,\\ \tilde{t}_1 = 0, \quad \tilde{t}_{N+1} + \widetilde{\Delta t}_{N+1} = \tau.\end{gathered}\right\} \tag{3.3}$$

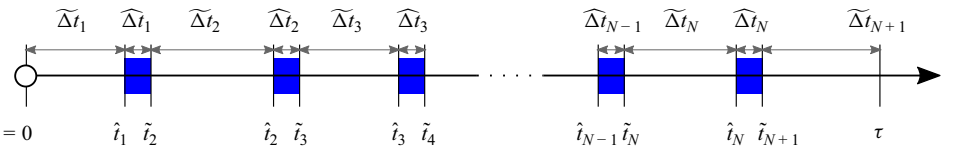

Figure 3. The entire analysis time τ is split into a number N of dissipation periods (indicated in blue) where a portion of the TPCL moves at velocities of $O(v_{cap})$, interspersed between $N+1$ equilibrium stages where the entire TPCL moves at velocities of at most $O(v_{cv})$.

In terms of notation used in the remainder of the analysis, variables annotated with a 'hat' correspond to properties associated with individual dissipation events (where parts of the TPCL are moving at $O(v_{cap})$), variables annotated with a 'tilde' correspond to properties associated with the system while in equilibrium (where the entire TPCL is moving at at most $O(v_{cv})$), and variables annotated with a 'bar' correspond to the entire advancing period τ. The decomposition of τ into separate dissipation and equilibrium stages is a key concept used in the subsequent energy analysis.

A number of mathematical constraints follow from the dynamic model of fluid movement described above. First, the analysis assumes that $v_{cv} \ll v_{cap}$. By assuming that the fluids are Newtonian with a stress defined by

$$T_M = -pI + \mu[\nabla \boldsymbol{v} + (\nabla \boldsymbol{v})^{\mathrm{T}}], \tag{3.4}$$

an order of magnitude analysis on the augmented Navier–Stokes equations (as defined by (2.1) and (2.2)) shows that capillary-driven fluid velocities can be limited by either viscous dissipation (i.e. $Ca \sim 1$) or momentum acceleration/advection inertial terms (i.e. $We \sim 1$) during any dissipation event. Hence a conservative estimate for the capillary-driven velocity scale is

$$v_{cap} = \min\left(\frac{\sigma}{\mu}, \sqrt{\frac{\sigma}{\rho\, h_{rough}}}\right). \tag{3.5}$$

In this expression and subsequent order of magnitude analyses, properties such as σ, μ and ρ are order of magnitude estimates only, which for most expressions can be taken as the maximum of the different phase properties existing within the CV. Equation (3.5) places a constraint on the maximum v_{cv} that can be used, given that $v_{cv} \ll v_{cap}$.

Interestingly, (3.5) predicts that capillary velocities are limited by inertial terms ($We \sim 1$) rather than viscous terms ($Ca \sim 1$) on most practical surfaces. To illustrate, for a water droplet within air advancing over a rough solid surface, the viscous limited velocity is $\sigma/\mu \approx 72\ \mathrm{m\ s^{-1}}$, while for all surface roughness values $h_{rough} \gtrapprox h_{rough,crit} = \mu^2/(\rho\sigma) = 14$ nm, the inertially limited velocity ($\sqrt{\sigma/(\rho\, h_{rough})}$) is smaller and hence will determine v_{cap}. Indeed, for a more typical surface roughness $h_{rough} = 10\ \mu\mathrm{m}$, (3.5) gives $v_{cap} \approx 3\ \mathrm{m\ s^{-1}}$. We consider the implications of this in more detail in § 4.3. Note that even though the local velocities existing during a dissipation event may be determined by a balance between capillary and inertial terms ($We \sim 1$), the Reynolds number for the motion near the surface roughness is not large ($Re \sim 20$ for the above $h_{rough} = 10\ \mu\mathrm{m}$ system). This means that the size of the region where velocities are $O(v_{cap})$ during dissipation events is only of $O(h_{rough})$, and importantly, these high velocities will not exist at the circumference of the CV, located at approximately r_{cv} from the TPCL.

A second constraint required by the dynamic model of fluid movement outlined above is that $\tau_{cap} \ll \tau$. We first note that the time taken for each dissipation event can be estimated from the interface velocity and distance travelled during each

event – $\widehat{\Delta t}_k = O(h_{rough}/v_{cap})$ – and that as there are N dissipation events occurring during τ, $\tau_{cap} = O(N\, h_{rough}/v_{cap})$. Recognising that the number of dissipation events occurring during the advance duration is $O(A_{cv}/h_{rough}^2)$ where $A_{cv} = X_{cv} l_{cv}$, and that $\tau = X_{cv}/v_{cv}$, leads to

$$\frac{\tau_{cap}}{\tau} = O\left(\frac{l_{cv}}{h_{rough}}\,\frac{v_{cv}}{v_{cap}}\right) \ll 1. \tag{3.6}$$

Equation (3.6) can always be satisfied provided that v_{cv} is small enough, which is obviously the case when determining θ_a as this angle is derived in the limit of $v_{cv} \to 0$. If the energy balance is being applied to moving interfaces, however, (i.e. $v_{cv} \neq 0$), then (3.6) places a constraint on the maximum applicable v_{cv}. This is discussed further in § 4.3.

Two final conceptual models concerning the continuous fluid movement occurring during the equilibrium stages of the flow have to be developed in order to apply the MMEB; these specify the velocity gradient and pressure, both of which relate to the fluid stress.

For the velocity gradient, we note that during equilibrium stages, the TPCL advances at a speed of $O(v_{cv})$ over the solid, resulting in a velocity discontinuity at the solid surface if the conventional continuum no-slip fluid boundary condition is applied. Indeed, velocity profiles that satisfy the Navier–Stokes equations and that are consistent with both a moving TPCL and the no-slip boundary condition are available (Moffatt 1964; Huh & Scriven 1971); however, these result in velocity gradients near that TPCL that increase as $1/r$ (where r is the distance to the TPCL). We find that integrating these gradients over the region surrounding the TPCL in our energy balance results in an energy dissipation term for non-zero v_{cv} that diverges logarithmically in an unphysical fashion, as others have found (Huh & Scriven 1971). Proposed solutions to this problem, which we invoke here, all involve removing or limiting the stress (equivalently velocity gradients) within the fluid at small distances (h_{mol}) from the TPCL. Various justifications for this limiting have been proposed (Huh & Scriven 1971; Joanny & de Gennes 1984; Petrov & Petrov 1992), but most revolve around a breakdown of the Newtonian or continuum model of a fluid at the TPCL where individual molecules or particles within the fluid must 'jump' along the solid. The implications of this limit are discussed further in § 4.3. Putting these concepts together, we hence estimate the velocity gradients existing within the fluid during the equilibrium stages as

$$\widetilde{\boldsymbol{\nabla}}\boldsymbol{v} = O\left(\frac{v_{cv}}{\max(r, h_{mol})}\right), \tag{3.7}$$

where as discussed, h_{mol} is a small length scale related to the molecular (or non-continuum) nature of the fluid.

For the continuous flow pressure variation, we perform an order of magnitude on the single-phase Navier–Stokes equations, recognising that pressure gradients may develop in response to viscous stress, momentum acceleration/advection and/or gravitational terms. This gives an expression for the pressure gradient in either fluid phase as

$$\begin{aligned}\widetilde{\boldsymbol{\nabla}}p &= O(\rho\, \boldsymbol{\nabla} \cdot \tilde{\boldsymbol{v}}\tilde{\boldsymbol{v}}) + O(\mu\, \nabla^2 \tilde{\boldsymbol{v}}) + O(\rho \boldsymbol{g}) \\ &= O\left(\frac{\rho v_{cv}^2}{\max(r, h_{mol})}\right) + O\left(\frac{\mu v_{cv}}{[\max(r, h_{mol})]^2}\right) + O(\rho g),\end{aligned} \tag{3.8}$$

where again the fluid stress has been limited within a distance of h_{mol} from the TPCL. Noting that the equilibrium stage fluid pressure $\tilde{p}$ is relative to some point in the

surrounding fluid far from the TPCL, and that under these slow flow conditions there is a potential pressure jump over the fluid interface due to the surrounding interface curvature of $O(\sigma/h_{surround})$, we model the pressure variation within the CV during the equilibrium stages as

$$\tilde{p} = O(\rho v_{cv}^2) + O\left(\frac{\mu v_{cv}}{\max(r, h_{mol})}\right) + O\left(\frac{\sigma}{h_{surround}}\right) + O(\rho g r_{cv}) + p_0, \tag{3.9}$$

where p_0 is some reference pressure located at a point away from the TPCL, but within the vicinity of the CV. All models describing the conceptual behaviour of the fluid phases during the equilibrium stages have now been defined.

For the solid phase, to apply the MMEB, we need models that describe how the solid velocities and stresses vary as the TPCL advances over the rough surface. In this study, we invoke the simplest possible model by assuming that velocities within the solid are everywhere zero. With this assumption the energy balance becomes independent of solid phase stresses. On physical grounds, zero velocities can be justified within the solid by assuming that it is a yield-stress (or plastic) material that does not experience a stress exceeding its yield-stress during the analysis time. In reality, this is probably justifiable for most solids used in engineering applications, but for soft solids used in (e.g.) biomedical applications, energy dissipation within the solid phase may be significant. This is certainly an area for future work that could be incorporated into the presented mechanical energy balance framework, but it is not advanced here.

3.3. *Applying the mechanical energy balance to the moving CV*

With the physical system defined and semi-quantitative models for how the materials within the CV behave as it advances over the rough solid, we can now apply the MMEB to find the advancing contact angle.

3.3.1. *Formulating the contact-angle mechanical energy balance*

We start by deriving the most general form of the contact-angle energy balance by applying (2.10) to the moving CV and integrating it over a time period from t_1 to t_2, giving

$$T_0(t_1, t_2) = \sum_{i=1}^{6} T_i(t_1, t_2), \tag{3.10}$$

where

$$T_0(t_1, t_2) = \frac{1}{A_{cv}}\left[E(t = t_2) - E(t = t_1)\right], \tag{3.11}$$

$$E(t) = \int_{V_{cv}} \left(\frac{1}{2}\rho v^2 + \rho\hat{\Phi}\right) \mathrm{d}V + \sum_{i<j} \sigma_{ij} A_{ij}, \tag{3.12}$$

$$T_1(t_1, t_2) = \frac{1}{A_{cv}} \int_{t_1}^{t_2} \int_{S_{cv}} \sum_{i<j} \sigma_{ij}\delta_{S,ij}\boldsymbol{n}_{cv} \cdot \boldsymbol{v}_{cv} \,\mathrm{d}S \,\mathrm{d}t, \tag{3.13}$$

$$T_2(t_1, t_2) = \frac{1}{A_{cv}} \int_{t_1}^{t_2} \int_{S_{cv}} \boldsymbol{n}_{cv} \cdot \frac{1}{2}\rho v^2 (\boldsymbol{v}_{cv} - \boldsymbol{v}) \,\mathrm{d}S \,\mathrm{d}t, \tag{3.14}$$

$$T_3(t_1,t_2)=\frac{1}{A_{cv}}\int_{t_1}^{t_2}\int_{S_{cv}}\boldsymbol{n}_{cv}\cdot\rho\hat{\Phi}(\boldsymbol{v}_{cv}-\boldsymbol{v})\,\mathrm{d}S\,\mathrm{d}t, \tag{3.15}$$

$$T_4(t_1,t_2)=-\frac{1}{A_{cv}}\int_{t_1}^{t_2}\int_{S_{cv}}\sum_{i<j}\sigma_{ij}\delta_{S,ij}\boldsymbol{n}_{S,ij}\boldsymbol{n}_{S,ij}:\boldsymbol{v}\boldsymbol{n}_{cv}\,\mathrm{d}S\,\mathrm{d}t, \tag{3.16}$$

$$T_5(t_1,t_2)=\frac{1}{A_{cv}}\int_{t_1}^{t_2}\int_{S_{cv}}T_M:\boldsymbol{v}\boldsymbol{n}_{cv}\,\mathrm{d}S\,\mathrm{d}t, \tag{3.17}$$

$$T_6(t_1,t_2)=-\frac{1}{A_{cv}}\int_{t_1}^{t_2}\int_{V_{cv}}T_M:\nabla\boldsymbol{v}\,\mathrm{d}V\,\mathrm{d}t. \tag{3.18}$$

In the derivation, use has been made of $\boldsymbol{I}:\boldsymbol{v}\boldsymbol{n}_{cv}=\boldsymbol{n}_{cv}\cdot\boldsymbol{v}$.

Next, defining the following notations that correspond to the entire, the kth equilibrium and the kth dissipation stages of the advance as

$$\bar{T}_i=T_i(t_1=0,t_2=\tau), \tag{3.19}$$

$$\tilde{T}_{i,k}=T_i(t_1=\tilde{t}_k,t_2=\tilde{t}_k+\widetilde{\Delta t}_k), \tag{3.20}$$

$$\hat{T}_{i,k}=T_i(t_1=\hat{t}_k,t_2=\hat{t}_k+\widehat{\Delta t}_k), \tag{3.21}$$

respectively for $i=0$ to 6, (3.10) is applied over the entire advance period from time 0 to τ to give

$$\bar{T}_0=\sum_{i=1}^{6}\bar{T}_i. \tag{3.22}$$

Recognising that $\bar{T}_i$ for $i=1$ to 6 are all integrals over the total time period, using (3.3) these terms can be written as sums of the corresponding terms from the equilibrium and dissipation stages, giving

$$\bar{T}_0=\sum_{i=1}^{6}\left(\sum_{k=1}^{N+1}\tilde{T}_{i,k}+\sum_{k=1}^{N}\hat{T}_{i,k}\right)=\sum_{i=1}^{6}\sum_{k=1}^{N+1}\tilde{T}_{i,k}+\sum_{k=1}^{N}\sum_{i=1}^{6}\hat{T}_{i,k}. \tag{3.23}$$

To simplify the final term, we apply the energy balance equation (3.10) to the kth dissipation period, giving

$$\hat{T}_{0,k}=\sum_{i=1}^{6}\hat{T}_{i,k}, \tag{3.24}$$

which, when substituted back into (3.23), leads to

$$\bar{T}_0=\sum_{i=1}^{6}\sum_{k=1}^{N+1}\tilde{T}_{i,k}+\sum_{k=1}^{N}\hat{T}_{0,k}. \tag{3.25}$$

This is the form of the energy balance that is used to evaluate the advancing contact angle. It expresses the total change in mechanical energy within the moving CV between the start and end of the advance ($\bar{T}_0$) as the sum of energy transfers happening during each of the $N+1$ equilibrium stages ($\tilde{T}_{i,k}$) plus the change in mechanical energy existing within the CV that occurs over each of the N dissipation events ($\hat{T}_{0,k}$). We now examine each of these terms, finding either their order of magnitude, or – for terms that prove to be significant – expressions that allow their quantitative evaluation in terms of system properties. This analysis is straightforward but detailed, and is presented in full in Appendix B.

3.3.2. *Final contact-angle mechanical energy balance*

With each term within the contact-angle energy balance evaluated, we substitute their expressions from (B2), (B6), (B13), (B15), (B17), (B19), (B23) and (B26) into (3.25) and gather like terms, giving

$$O(\rho v_{cv}^2 h_{rough}) + O(\rho g l_{cv} h_{rough}) + O\left(\frac{\sigma h_{rough}}{X_{cv}}\right) = O(\rho g h_{rough}^2) + O(\rho v_{cv}^2 r_{cv}) + O(\rho g r_{cv}^2) + O\left(\sigma \frac{h_{rough}}{l_{cv}}\right) + O(\mu v_{cv}) + O\left(\frac{\sigma r_{cv}}{h_{surround}}\right) + O\left[\mu v_{cv} \ln\left(\frac{r_{cv}}{h_{mol}}\right)\right] + \widehat{\Delta\sigma} - \sigma_{12}\cos\theta_a + \sigma_{2C} - \sigma_{1C}. \tag{3.26}$$

Neglecting any terms that are relatively small due to the length scales equation (3.1) yields

$$\widehat{\Delta\sigma} - \sigma_{12}\cos\theta_a + \sigma_{2C} - \sigma_{1C} = O(\rho v_{cv}^2 r_{cv}) + O(\rho g r_{cv}^2) + O\left[\mu v_{cv} \ln\left(\frac{r_{cv}}{h_{mol}}\right)\right]. \tag{3.27}$$

Equivalently, this contact-angle energy balance can be expressed as

$$\sigma_{12}\cos\theta_a = \widehat{\Delta\sigma} + \sigma_{2C} - \sigma_{1C}, \tag{3.28}$$

under conditions where the following inequalities hold:

$$\frac{\rho v_{cv}^2 r_{cv}}{\sigma}, \frac{\rho g r_{cv}^2}{\sigma}, \frac{\mu v_{cv}}{\sigma} \ln\left(\frac{r_{cv}}{h_{mol}}\right) \ll 1. \tag{3.29}$$

Three new surface energies are used in (3.28). The compound surface energies

$$\sigma_{1C} = \sum_{i<j} \sigma_{ij} \frac{A_{1C,ij}}{A_{cv}} \quad \text{and} \quad \sigma_{2C} = \sum_{i<j} \sigma_{ij} \frac{A_{2C,ij}}{A_{cv}}, \tag{3.30a,b}$$

measure the surface energy of all interfaces associated with the rough solid, on the leaving (behind and to the left of the TPCL) and entering (in front and to the right of the TPCL) sides of the advancing CV, respectively. We note that in addition to energy increases caused by the roughness increasing the specific solid surface area, these compound surface energies also account for any micro-bubbles or droplets that could possibly be contained within the surface structures. For the leaving energy (σ_{1C}), these could be formed during the discussed dissipation events that occur as the TPCL sweeps over rough solid, while for the entering energy (σ_{2C}), these could be pre-existing within the surface roughness, possibly as a result of previous wetting processes (such as receding back over a previously wetted surface). Additionally, the specific dissipation event surface energy change is defined as

$$\widehat{\Delta\sigma} = \sum_{k=1}^{N} \sum_{i<j} \sigma_{ij} \frac{\widehat{\Delta A_{ij}}_k}{A_{cv}}. \tag{3.31}$$

This variable represents the sum of changes to potential surface energies occurring within the CV over all capillary-driven dissipation events, per projected area of solid traversed. This variable has a magnitude of $O(\sigma)$ and is key in predicting roughness-induced CAH.

3.3.3. *Interpretation of specific dissipation event surface energy change* $\widehat{\Delta\sigma}$

The specific dissipation event surface energy change $\widehat{\Delta\sigma}$ as defined above is the sum of all surface energy changes occurring within the CV over each interface slip event. However, consistent with the physical model of how the contact line advances over the rough solid as outlined in § 3.2, we hypothesise that these surface energy changes are dissipated to heat (via viscous stresses) during each slip event, resulting in a negative $\widehat{\Delta\sigma}$. Hence an alternative nomenclature for this term that is consistent with this contact-line movement model and previous literature (e.g. Joanny & de Gennes 1984) is to define the specific dissipation per projected area of solid traversed due to surface roughness as $D \approx -\widehat{\Delta\sigma}$. In this subsubsection, we show how this relationship formally holds true by performing an order of magnitude analysis on an energy balance conducted over all dissipation slip events occurring during the advance period.

In order to perform this analysis, we need models for how the materials within the CV behave during the dissipation periods. As for the equilibrium periods, we assume that the solid does not deform (following the justifications from § 3.2), giving $\boldsymbol{v} = 0$ within the solid during these times. For the fluids, we require a description of the velocity $\hat{\boldsymbol{v}}$, velocity gradient $\widehat{\boldsymbol{\nabla}\boldsymbol{v}}$ and pressure $\hat{p}$ existing during these times. For the velocity, noting that the continuous equilibrium velocities still exist within the dissipation periods, and assuming that significant capillary-driven velocities exist only within a region of size $O(h_{rough})$ local to each dissipation event (as Re for these motions is not large), we define

$$\hat{\boldsymbol{v}}(\boldsymbol{x}) = \begin{cases} \tilde{\boldsymbol{v}} + O(v_{cap}) & \text{if } r_{cap} < O(h_{rough}), \\ \tilde{\boldsymbol{v}} & \text{otherwise,} \end{cases} \tag{3.32}$$

where $r_{cap} = |\boldsymbol{x} - \boldsymbol{x}_{cap}|$ is the distance to the centre of the relevant kth dissipation event, and $\boldsymbol{x}_{cap}$ is the location of the particular kth dissipation event that is centred on the centreline of the CV. (For notational simplicity here and in subsequent dissipation event model definitions, we do not indicate what specific dissipation event variables such as $\hat{\boldsymbol{v}}$, $\boldsymbol{x}_{cap}$ and r_{cap} refer to.) For the velocity gradient, we similarly define

$$\widehat{\boldsymbol{\nabla}\boldsymbol{v}}(\boldsymbol{x}) = \begin{cases} \widetilde{\boldsymbol{\nabla}\boldsymbol{v}} + O\left(\dfrac{v_{cap}}{\max(r_{cap}, h_{mol})}\right) & \text{if } r_{cap} < O(h_{rough}), \\ \widetilde{\boldsymbol{\nabla}\boldsymbol{v}} & \text{otherwise,} \end{cases} \tag{3.33}$$

where as per the equilibrium velocity gradient model of (3.7), we limit the stress generated at the moving TPCL that is within $O(h_{mol})$ of the solid. Finally, for pressure, we perform another order of magnitude analysis on the Navier–Stokes equations, but now recognise that capillary induced pressure changes occur over the interface that is deforming over length $O(h_{rough})$ during these times, giving

$$\hat{p}(\boldsymbol{x}) = \begin{cases} \tilde{p} + O(\rho v_{cap}^2) + O\left(\dfrac{\mu v_{cap}}{\max(r_{cap}, h_{mol})}\right) + O\left(\dfrac{\sigma}{h_{rough}}\right) & \text{if } r_{cap} < O(h_{rough}), \\ \tilde{p} & \text{otherwise.} \end{cases} \tag{3.34}$$

This completes the dissipation event material specifications.

The dissipation event energy analysis now largely mirrors that conducted for the equilibrium stages (as detailed in §§ B.3–B.8) by summing the individual dissipation event energy balances of (3.24) over all N dissipation events. The details of this analysis are

contained within Appendix C, with the final result being

$$\widehat{\Delta\sigma} = O\left(\frac{\tau_{cap}}{\tau}\sum_{i=1}^{6}\sum_{k=1}^{N+1}\tilde{T}_{i,k}\right) + O(\rho v_{cv}^2\, h_{rough}) + O(\rho g\, h_{rough}^2)$$
$$+ O\left(\frac{\rho v_{cap}^2\, h_{rough}^2}{l_{cv}}\right) + O\left(\frac{\rho g\, h_{rough}^3}{l_{cv}}\right) + O\left(\sigma\,\frac{h_{rough}}{l_{cv}}\right)$$
$$+ O\left(\mu v_{cap}\,\frac{h_{rough}}{l_{cv}}\right) + O\left[\mu v_{cap}\ln\left(\frac{h_{rough}}{h_{mol}}\right)\right]. \tag{3.35}$$

Under conditions for which the inequalities of (3.29) hold, the equilibrium terms represented by $\sum_{k=1}^{N+1}\tilde{T}_{i,k}$ in the above have a maximum magnitude of $O(\sigma)$, which is the same as that of $\widehat{\Delta\sigma}$. As $O(\tau_{cap}/\tau) \ll 1$ via (3.6), it follows that the equilibrium terms make no significant contribution to (3.35) and can be neglected. For the remaining terms, using the length scales assumption (3.1) in combination with (3.29) yields, after simplifications,

$$\widehat{\Delta\sigma} = O\left(\frac{\rho v_{cap}^2\, h_{rough}^2}{l_{cv}}\right) + O\left[\mu v_{cap}\ln\left(\frac{h_{rough}}{h_{mol}}\right)\right]. \tag{3.36}$$

Tracing back through the dissipation energy analysis presented in Appendix C shows that the first and second terms on the right-hand side of (3.36) represent the transport of kinetic energy (and associated pressure work) through the ends of the CV due to dissipation event velocities, and the viscous dissipation of energy that is converted to heat around the moving TPCL during dissipation events, respectively. The ratio of these two terms depends on *Re* as well as various length scale ratios, so that in general neither can be assumed to be dominant. The second term directly represents energy conversion to heat during the capillary-driven dissipation events, as envisaged. While the first term does not relate directly to energy dissipation, it does represent the transport of energy through the ends of the CV and hence parallel to the TPCL. As the analysis shows that no significant energy transport occurs over the circumference of the CV during the dissipation events, the energy represented by the first term in (3.36) remains within the vicinity of the contact line, and so will eventually be dissipated to heat via the second term in the same equation, but in an adjacent CV. Hence, overall (3.36) shows that the energy liberated by surface changes that occur during each dissipation event is dissipated to heat within the vicinity of the TPCL, and we are justified in using the nomenclature $D = -\widehat{\Delta\sigma}$ that states that the specific energy dissipation per area travelled due to surface roughness can be calculated from the changes in interfacial energies that occur over each of the dissipation 'stick–slip' events. It should be reiterated, however, that the discussion in this section does not change the way in which $\widehat{\Delta\sigma}$ (or equivalently $-D$) is evaluated, being defined solely in terms of surface energy changes that occur over all dissipation events. Indeed, a key result of this study is that D can be calculated based solely on these surface energy changes, rather than needing to know the transient details of each individual dissipation event.

4. Discussion

4.1. *Summary of key results*

The contact-angle mechanical energy balance equations are summarised in table 1. The requirements of inequality (3.29) have been combined with previous length scale

assumptions and interpreted as conditions on r_{cv} and v_{cv}. Additionally, $O(l_{cv}) = O(r_{cv})$ is applied throughout. The limiting CV size variable $r_{cv,grav}$ is the capillary length that in this analysis has originated from limiting the transport of gravitational potential energy during the equilibrium stages of the energy balance. The three limiting CV velocities $v_{cv,ke}$, $v_{cv,vis}$ and $v_{cv,cap}$ have originated from limiting the transport of kinetic energy through the CV boundaries during the equilibrium stages, limiting the rate of viscous dissipation occurring at a molecular level around the moving TPCL during the equilibrium stages, and ensuring that the duration of dissipation events occurring within the CV is small compared to the duration of interface movement, respectively.

As shown in the table, the advancing angle analysis can also be applied to provide an expression for the receding contact angle θ_r of phase ①. As per figure 2, when phase ① is advancing over the solid, phase ② is receding. Hence substituting $\theta_a = \pi - \theta_{r,2}$ into (4.2), where $\theta_{r,2}$ is the receding angle of phase ②, and then swapping all indices ($1 \leftrightarrow 2$) results in (4.3). Note that to distinguish between the two wetting processes, D_a and D_r have been defined individually as the specific dissipations occurring during the advancing and receding of phase ①, respectively, noting, however, that both are calculated using the same equation but applied at different times. Note also that while σ_{2C} and σ_{1C} have not been given specific 'a' and 'r' subscripts, they will not necessarily be the same between an interface's advance and recede. For example, if a liquid does not completely dewet a surface when receding (and microdroplets are left behind), then σ_{2C} during the recede will be different than it was during the first advance. Similarly, σ_{1C} may be different between an advance and recede if (say) microbubbles/microdroplets formed under phase ① during the advance dissolve/evaporate prior to the interface receding over the same region again. If, however, σ_{2C} and σ_{1C} do remain the same before and after an interface advance and recede combination, then together (4.2) and (4.3) show that the cosine of the total CAH is given by

$$\sigma_{12}(\cos\theta_r - \cos\theta_a) = D_a + D_r = D_t, \tag{4.1}$$

where D_t is the total dissipation occurring over the advance and recede combination. While this equation (or slight variations thereof) has been employed to model or analyse CAH in previous works (e.g. de Gennes 1985; Reyssat & Quéré 2009; Ramiasa *et al.* 2013; Butt *et al.* 2017), we do emphasise that it is valid only if σ_{2C} and σ_{1C} are unchanged after an entire advance and recede cycle.

4.2. *Application to various wetting regimes*

We now analyse various wetting regimes using the contact-angle mechanical energy balance.

4.2.1. *Young's*

For a fluid advancing over a perfectly flat surface (that satisfies our other system constraints), the phase ① compound surface energy is $\sigma_{1C} = \sigma_{1s}$, the phase ② compound surface energy is $\sigma_{2C} = \sigma_{2s}$, and the specific roughness dissipation rate is $D_a = 0$ as no dissipation events occur during the TPCL advance. Application of (4.2) gives $\sigma_{12}\cos\theta_a = \sigma_{2s} - \sigma_{1s}$, or via Young's equation, $\theta_a = \theta_e$. Note that this relationship applies also to the receding angle.

We have

$$\sigma_{12}\cos\theta_a = \sigma_{2C} - \sigma_{1C} - D_a, \tag{4.2}$$

$$\sigma_{12}\cos\theta_r = \sigma_{2C} - \sigma_{1C} + D_r, \tag{4.3}$$

subject to

$$h_{mol} \ll h_{rough} \ll r_{cv} \ll h_{surround}, r_{cv,grav}, \tag{4.4}$$

$$v_{cv} \ll \min\left(v_{cv,ke}, v_{cv,vis}, v_{cv,cap}\right), \tag{4.5}$$

where

$$\sigma_{1C} = \sum_{i<j}\sigma_{ij}\frac{A_{1C,ij}}{A_{cv}} \quad \text{and} \quad \sigma_{2C} = \sum_{i<j}\sigma_{ij}\frac{A_{2C,ij}}{A_{cv}}, \tag{3.30a,b}$$

$$D_{a/r} = -\sum_{k=1}^{N}\sum_{i<j}\sigma_{ij}\frac{\widehat{\Delta A}_{ijk}}{A_{cv}}, \tag{4.6}$$

$$v_{cap} = \min\left(\frac{\sigma}{\mu}, \sqrt{\frac{\sigma}{\rho\, h_{rough}}}\right), \tag{3.5}$$

$$v_{cv,ke} = \sqrt{\frac{\sigma}{\rho r_{cv}}}, \tag{4.7}$$

$$v_{cv,vis} = \sqrt{\frac{\sigma}{\mu \ln(r_{cv}/h_{mol})}}, \tag{4.8}$$

$$v_{cv,cap} = v_{cap}\frac{h_{rough}}{r_{cv}}, \tag{4.9}$$

$$r_{cv,grav} = \sqrt{\frac{\sigma}{\rho g}}. \tag{4.10}$$

Table 1. Equation summary for the contact-angle mechanical energy balance.

4.2.2. *Wenzel*

The Wenzel regime here means that both phases completely wet their corresponding compound surfaces. Hence during advance, the phase ① compound surface energy is $\sigma_{1C} = r\sigma_{1s}$ and the phase ② surface energy is $\sigma_{2C} = r\sigma_{2s}$, where r is the roughness or specific solid area (total solid area per projected solid area). Application of (4.2) gives $\cos\theta_a = r\cos\theta_e - D_a/\sigma_{12}$, which is consistent with Wenzel's equation, but augmented by a roughness dissipation term. Here, increasing the roughness r can either increase or decrease the advancing angle, depending on θ_e; however, increasing the roughness dissipation D_a always increases the contact angle.

4.2.3. *Cassie–Baxter*

In the general Cassie–Baxter case, f_1 and f_2 are defined as the wetted and non-wetted liquid areas under the droplet per projected area, respectively, with r defined as per the Wenzel case. Under these conditions, the phase ① compound surface energy is $\sigma_{1C} = -f_1\sigma_{12}\cos\theta_e + f_2\sigma_{12} + r\sigma_{2s}$, and the phase ② compound surface energy is $\sigma_{1C} = r\sigma_{2s}$.

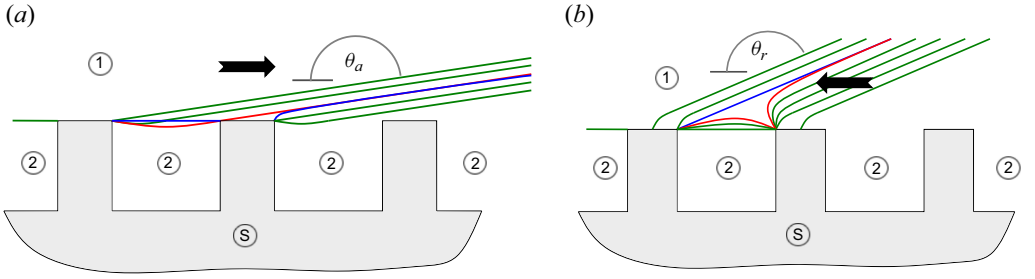

Figure 4. Schematics illustrating how the various interface areas change during the dissipation events occurring when a Fakir droplet/TPCL (*a*) advances or (*b*) recedes over a rough surface containing flat-topped poles. In each case, the fluid/fluid interface (A_{12}) shape that immediately precedes the dissipation event is indicated in red, the fluid/fluid interface shape that immediately follows the dissipation event is indicated in blue, and the other green fluid/fluid interface shapes represent equilibrium stages where the interface is moving in a continuous manner. Note that the schematics are a two-dimensional representation of a three-dimensional process.

Substituting into (4.2) gives $\cos\theta_a = f_1\cos\theta_e - f_2 - D_a/\sigma_{12}$, which is consistent with the analysis of Cassie & Baxter (1944), but again augmented with a dissipation term.

4.2.4. *Fakir droplets*

For a droplet resting on the top of flat 'pole' structures (e.g. super-hydrophobic 'Fakir' droplets existing on photolithography-based surfaces) the above Cassie–Baxter equation can be combined with a simple model for the interface deformation occurring during dissipation events to produce a quantifiable model of CAH.

First, we note that for this particular wetting regime, provided that the inherent Young's angle for the fluid combination is high (say $\theta_e \gtrapprox 90^\circ$), the area fraction of the projected solid surface covered in poles will be $\phi = f_1 = 1 - f_2$. Applying this relationship to the previous Cassie–Baxter theory gives

$$\cos\theta_a = \cos\theta_{CB} - D'_a \quad \text{and} \quad \cos\theta_r = \cos\theta_{CB} + D'_r, \tag{4.11a,b}$$

where $\cos\theta_{CB} = \phi(1+\cos\theta_e) - 1$ introduces the well-known equilibrium Cassie–Baxter angle for this system, and the dissipations have been non-dimensionalised using $D'_{a/r} = D_{a/r}/\sigma_{12}$.

To develop expressions for the two dissipations, we refer to the schematics shown in figure 4 that illustrate how the interfacial areas change as the TPCL advances in a 'stick–slip' manner.

Focusing first on the advancing case, when the fluid/fluid interface just touches the next pole (indicated by the red interface profile in figure 4*a*), the local contact angle is immediately in excess of its Young's value, causing the local TPCL to rapidly slip across the top of the pole. Indeed, the interface does not stop moving until the majority of the pole top area is covered (indicated by the blue shape profile in the figure). This process, which has been observed via high-speed photography (Jiang *et al.* 2019), results in dissipation. Specifically, over this event, the area on the top of one pole changes from being wetted by phase ② to phase ①, and the fluid/fluid interface is reduced by an amount that is almost equal to the top area of the pole. Applying these concepts to (4.6) gives

$$D'_a = \phi(\beta + \cos\theta_e), \tag{4.12}$$

with β defined as the decrease in A_{12} occurring during a single advancing dissipation event, normalised by the top area of one pole. From the above discussion we expect $\beta \approx 1$.

The receding dissipation event is slightly more complex. As observed (Schellenberger *et al.* 2016; Jiang *et al.* 2019) and indicated in figure 4(*b*), for the hydrophobic liquids considered here, the local TPCL actually moves continuously across each pole top during a recede, only 'depinning' from the pole (and dissipating energy) after the liquid contact area has almost reduced to a single point (indicated by red in figure 4*b*). After being released from the pole, the fluid/fluid interface rapidly adopts an equilibrium configuration, as indicated by the blue profile in figure 4(*b*). Examining the change in interfacial areas that occurs over this receding dissipation event, we see that they are primarily limited to a decrease in A_{12}, which we again express as a multiple (α) of the top area of the pole, giving

$$D_r' = \phi\alpha. \tag{4.13}$$

Given the kinematics of the event, we expect α to be a small but positive number.

Equations (4.11)–(4.13) relate the contact angles of Fakir droplets to the geometric parameters α and β that describe the receding and advancing dissipation events, respectively. In the limiting cases of $\beta = 1$ and $\alpha = 0$, the equations predict that $\theta_a = 180^\circ$ and $\theta_r = \theta_{CB}$, being angles that are approximately in line with measurements. Delving deeper, however, we can use (4.11)–(4.13) to find the geometric parameters α and β that produce the measured θ_a and θ_r for Fakir wetting, suggesting a method for predicting these angles for similar wetting systems. Table 2 shows these data for water wetting a hydrophobic surface structured with a staggered array of high-aspect-ratio posts, as measured by Öner & McCarthy (2000). Three surface modifications were tested, giving three different inherent contact angles (all $\theta_e > 98^\circ$), with all having very low inherent CAH ($<9^\circ$). The calculated α values vary from 0.17 to 0.2, and the β values vary from 0.93 to 0.98, both of which are in line with theoretical expectations, and both in narrow ranges suggesting that average parameters could be used to predict apparent contact angles for similar hydrophobic systems. A broader range of experimental data is analysed in the supplementary material available at https://doi.org/10.1017/jfm.2024.317 (see '1. Additional Fakir wetting data'), showing that in general, α values range between approximately 0.2 and 1.5, and β values between 0.7 and 1, as a function of surface structure, structure arrangement and inherent contact angle.

4.2.5. *General application to predict contact angles*

In general, the specific roughness dissipation D_a and phase ① compound surface energy σ_{1C} formed during an interface advance (equivalently D_r and σ_{2C} during recede) cannot be guessed from the solid topology alone and instead must be modelled from an understanding of the fluid dynamics occurring within the CV, or measured. Additionally, the phase ② compound surface energy σ_{2C} during advance (σ_{1C} during recede) depends on the history of the surface and must similarly be modelled or measured. Hence for wetting regimes that are more complex than those analysed above, the contact-angle equation (4.2) is a framework within which results from dynamic interfacial modelling or measurements can be incorporated for specific combinations of solid topologies and fluid phases. In a companion paper (Kumar & Harvie 2024), we use numerical simulations of roughness-scale interface dynamics during Wenzel wetting to predict CAH, finding excellent agreement with published experimental results. These simulations use no fitting parameters. Additionally, in Kumar, Mulvaney & Harvie (2024), we use contact-angle measurements on a variety of randomly and periodically structured surfaces wetting in

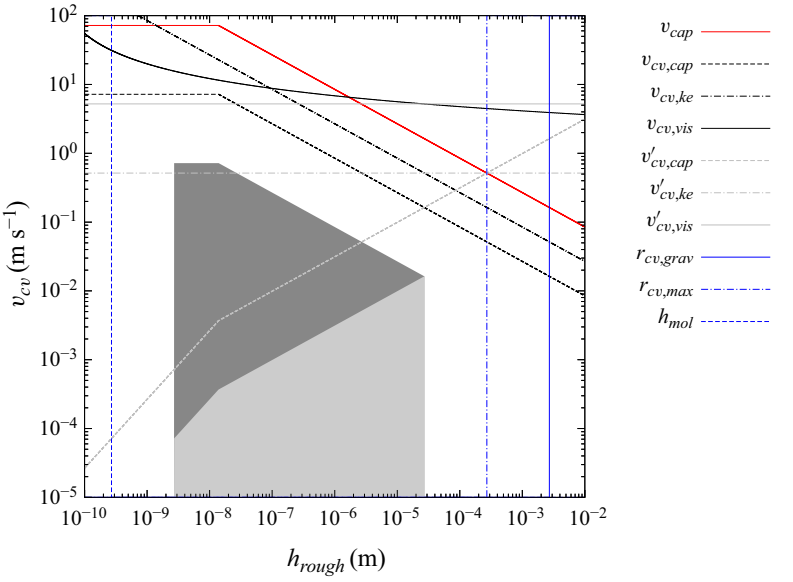

Figure 5. Regions of validity (shaded) for the contact-angle energy analysis based on a typical water/air system. The velocity limits $v_{cv,cap}$, $v_{cv,ke}$ and $v_{cv,vis}$, and the entire shaded validity region (dark grey plus light grey), assume that the CV size depends on the solid roughness according to $r_{cv}/h_{rough} = 10$. Conversely, the velocity limits $v'_{cv,cap}$, $v'_{cv,ke}$ and $v'_{cv,vis}$, and the light grey validity region, assume that the CV size is constant at the maximum allowable value of $r_{cv} = r_{cv,max} = r_{cv,grav}/10$.

the Wenzel regime to develop correlations for $D_{a/r}$, while also using the framework to determine under what conditions alternative wetting states may occur, thus delimiting the validity range for the results.

4.3. *Range of validity*

A strength of this analysis is that (4.4) and (4.5) specify the conditions under which (4.2) is valid. Continuing the discussion from § 3.2, we examine what physical limitations these conditions place on applying the theory to the common water/air system, with results shown in figure 5.

In terms of length scales, evaluating $r_{cv,grav}$ from (4.10) requires that $r_{cv} \ll r_{cv,grav} = 2.7$ mm, which is satisfied if we adopt $r_{cv} \lessapprox 0.27$ mm for the water system (i.e. one order of magnitude less). From the separation of length scales in (4.4), this in turn places an upper constraint on the roughness applicable under the theory of $h_{rough} \lessapprox 27$ μm, which is indicated by the right-hand bound of the shaded area in figure 5. Hence gravitational effects place an upper limit on the size of roughness applicable under this theory. At the small scales, we also require that $h_{mol} \ll h_{rough}$, and given that the molecular size of water is approximately 0.27 nm, this places a lower limit on h_{rough} of approximately 2.7 nm, as indicated by the left-hand bound of the shaded area in figure 5. Note that some theories use a larger length cut-off of 100 nm in their analysis, citing the influence of van der Waals and double-layer forces at these length scales (de Gennes 1985); while still continuum forces, these are not accounted for in our hydrodynamically based framework. Non-continuum effects such as thermal fluctuations that could influence interface topologies at very small length scales are also not considered. Hence, while the lower roughness size limit of this

theory requires further validation, overall the conclusion is that CAH can be significant even for surfaces that have very small-sized roughness (at least in an engineering sense), a conclusion that is supported by experiments (Delmas, Monthioux & Ondarçuhu 2011; Fetzer & Ralston 2011; Ramiasa *et al.* 2013).

In terms of the speed at which the CV can travel for the theory still to be valid (i.e. v_{cv}), the constraints partly depend on how the size of the CV is defined, or equivalently, at what distance from the solid (or TPCL) we are measuring the 'macroscopic' advancing angle θ_a. We consider two scenarios: in the first, the CV size (or measurement distance) decreases with h_{rough} such that $r_{cv}/h_{rough} = 10$; in the second, the CV size (or measurement distance) is kept constant at the maximum value of $r_{cv} = 0.27$ mm as determined by (4.4). The various limiting velocities corresponding to the decreasing CV size case are indicated by $v_{cv,cap}$, $v_{cv,ke}$ and $v_{cv,vis}$ in figure 5, while the limiting velocities corresponding to the constant CV size case are indicated by $v'_{cv,cap}$, $v'_{cv,ke}$ and $v'_{cv,vis}$. Similarly, the ranges of theory validity are shown in the figure by the entire shaded region for the decreasing CV case, and by the light shaded region for the constant CV case.

For both CV size (or measurement distance) scenarios, the capillary velocity constraint – which is an interpretation of (3.6) and requires that the total dissipation event time during the advance (τ_{cap}) is less than the total advance time (τ) – limits the advance velocity over the entire range of applicable roughness scales. As was discussed in § 3.2 and shown in figure 5, the capillary velocity v_{cap} for this water system increases as h_{rough} decreases, reaching $\sim$72 m s^{-1} below $h_{rough} = h_{rough,crit} \approx 14$ nm. For the decreasing CV size scenario, this velocity constraint allows v_{cv} to remain at practically large values (of $\sim$0.72 m s^{-1}) even at the lowest limit of applicable h_{rough}. For the constant CV scenario, however, the capillary velocity constraint decreases the viable v_{cv} as h_{rough} decreases, reaching $\sim$70 μm s^{-1} at the lowest applicable $h_{rough} \approx 2.7$ nm. Note that the link between measurement distance (or CV size) and contact angle has been made previously in the context of viscous-dissipation-based dynamic contact-angle models (e.g. de Gennes 1985).

A practical implication of this result is that for most surface roughness sizes and macroscopic angle measurement distances, there is a large range of interface velocities under which the interface will adopt its static (rather than dynamic) advancing angle. At the highest valid solid roughnesses, which are in the tens of microns range, the advancing angle will equal the static angle until the interface is moving faster than several cm s^{-1}. Conversely, at the lowest valid roughnesses, the maximum advance velocity at which the contact angle equals its static value depends on the angle measurement distance. However, even using the largest measurement distance combined with the smallest roughness, the maximum applicable advance velocity is still approximately 0.1 mm s^{-1}, which is certainly an experimentally accessible value for performing contact-angle measurements. In general, these results emphasise that for most chemically homogeneous/inert surfaces used in engineering applications, CAH depends more on surface roughness topology than interface velocity.

As discussed previously, for the constant CV size scenario – that is, the largest angle measurement distance, which is also arguably the most experimentally relevant – the upper velocity constraint is determined by $v'_{cv,cap}$, which ensures that all dissipation events occur independently in time. It is possible that this constraint could be relaxed if a different approach to the energy balance were adopted, specifically allowing several spatially independent dissipation events to occur concurrently. This route is more mathematically onerous, but could extend the theory to faster velocities in cases where the CV size

(measurement distance) is macroscopic (i.e. mm) and the roughness much smaller. Note that if the $v'_{cv,cap}$ restraint were relaxed, then the next constraint on the dynamic contact angle would come from $v'_{cv,ke}$, which is related to kinetic energy transport through the CV volume, rather than viscous dissipation ($v'_{cv,vis}$). Interestingly, previous theories have used viscous or molecular energy dissipation occurring around the TPCL to predict dynamic contact angles (Moffatt 1964; Huh & Scriven 1971; Voinov 1976; de Gennes 1985; Petrov & Petrov 1992); however, the present energy conservation framework suggests that kinetic energy transport should be considered as well (or instead).

It is interesting that aside from these length scale and velocity constraints, there is no reference to the absolute size of the surface roughness contained within the energy analysis. While models of D, σ_{1C} and σ_{2C} may in some cases depend on the absolute size of the surface roughness, it is likely that for many fluid combinations and solid topologies, they depend only on the topology of the roughness. As discussed in the Introduction, this is consistent with a growing number of observations (Öner & McCarthy 2000; Dorrer & Rühe 2008; Li *et al.* 2016; Jiang *et al.* 2019).

4.4. *Other model limitations*

In addition to the advance velocity, roughness size and CV size constraints discussed in the previous subsection, other assumptions used in the derivation of the contact-angle energy balance will not be valid for some systems, but could form avenues for future work.

Inherent in the contact-angle framework and enabling MMEB presented in § 2 is the assumption that there is no irreversible work involved in interface creation or destruction. This implies that the underlying smooth surface has no inherent hysteresis. Physically, irreversibilities could be present in a system due to chemical or molecular effects associated with interface formation, including energy losses due to surfactant adsorption or other surface-based molecular rearrangements. In the context of dynamic contact-angle modelling, work has been done to incorporate molecular dissipation and adsorption when predicting advancing contact angles (e.g. Blake & Haynes 1969; de Gennes 1985; Brochard-Wyart & de Gennes 1992; Karim 2022). Following this work and recognising the parallels between these interfacial formation irreversibilities and dissipation due to TPCL jumps, it is likely that this irreversible interfacial work would appear in the contact-angle energy balance as a dissipation term that is in addition to the hydodynamically based D, but this does require reformulation of the MMEB and application to the moving contact-line problem to show rigorously. A further assumption used by the model is that the solid is chemically homogeneous. This assumption could be relaxed in a straightforward manner by including more than one solid interface type in the contact-angle energy analysis.

Another limitation of the presented work is that the fluids are assumed to be incompressible, and no dissolution or evaporation of the fluids is permitted. Both of these assumptions are physically limiting when one of the phases is a gas. Physically, a gas will behave differently to a liquid in cases where a micro-bubble is formed within the solid roughness, caused by the specific dynamics of the fluid interface as it advances over solid defects. Within a formed micro-bubble, the Laplace pressure may be high ($O(\sigma/h_{rough})$, depending on the specific bubble geometry, however), which will cause the density of gas to increase and hence the volume of the micro-bubble to decrease. How significant these affects are depends on the bubble size, interfacial tension and gas equation of state. Further, high pressures within the bubble will drive gas dissolution into the surrounding fluid phase, further reducing the volume of the formed micro-bubbles. These changes to the micro-bubble size will in turn affect the leaving compound solid surface energy σ_{1C},

affecting the predicted advancing contact angle. In terms of the energy framework, fluid compressibility could be implemented quite easily by relaxing the $\boldsymbol{\nabla} \cdot \boldsymbol{v} = 0$ constraint used when evaluating the boundary pressure work terms. Gas dissolution is more complex, however, as this process is transient, so the framework would need to recognise over what time scale the dissolution process is taking place, and hence where in the energy balances the changes in (particularly) interfacial energy should occur. Micro-droplet evaporation is a related phenomenon not accounted for by the theory that could also change σ_{1C} and σ_{2C} depending on the wetting history of the solid surface and volatility of the fluids. It would be interesting to account for dissolution and evaporation effects within this framework as both introduce a transient or history effect to the wetting behaviour of the system. Again, this suggests avenues for future theoretical and experimental research.

A further limitation of the theory relates to the size of roughness considered. As presented, the roughness is characterised by a single length scale h_{rough} that represents both the height of surface defects and the spacing between them. An extension to this theory could distinguish between these two length scales, allowing a more tailored analysis of surfaces composed of a dilute number of strong defects. A second assumption relating to the size of the defects is that only one length scale is considered in the analysis, whereas real surfaces (particularly biological inspired super-hydrophobic surfaces) can possess a hierarchical range of roughnesses (Feng *et al.* 2002). A potential extension of the theory would be to use a cascade of CV sizes to predict the CAH at each length scale, with the interfacial modelling at each length scale determined from CAH predictions performed using smaller length scale CVs. In this way, the macroscopic CAH range could be determined from knowledge of roughness topologies at each length scale.

Finally, the stress model for the solid material used in this study effectively implies that there are no energy changes occurring within the CV that are related to the solid phase. More complex solid stress models could certainly be incorporated into the framework, representing (for example) the advance of fluids over soft or semi-liquid materials. Introducing deformable solids would not only introduce additional dissipation, but would also require additional dynamical modelling or measuring of the fluid, solid and interfacial behaviours occurring around the TPCL. This is also the topic of ongoing work.

4.5. *Relationship to other theories of roughness-induced CAH*

As alluded to in the Introduction, the present theory answers many questions that were hitherto open in the roughness-induced wetting field.

For several decades, there has been controversy regarding the validity and applicability of the Wenzel and Cassie–Baxter equations, with one recent review even suggesting that these equations 'must not be used in scientific articles' (Erbil 2021). The present theory, however, shows that these angles represent the zero-dissipation limits of moving contact lines in their respective wetting regimes, so both are important in locating and defining their respective CAH ranges. As a related question, there has long been an uncomfortable relationship between the use of thermodynamics and energy conservation in predicting CAH. In the present context, thermodynamic analysis involves choosing system conditions that minimise the free energy of a system. In agreement with recent analysis (Shardt & Elliott 2020), we contend that thermodynamics is not relevant for predicting CAH as by definition the CAH range is delimited by the advancing and receding angles, and these angles, again by definition, require the TPCL to move. The energy transfers that occur during interface movement are constrained by the kinematics of the interface shapes and fluid flow, as well as by energy conservation, rather than being

θ_e	θ_a	θ_r	θ_{CB}	α	β	D'_a	D'_r	D'_t
98	173.7	138.0	141.7	0.17	0.98	0.209	0.042	0.251
104.5	173.3	139.7	144.4	0.20	0.97	0.181	0.050	0.231
114.5	169.3	143.7	148.6	0.19	0.93	0.129	0.048	0.177

Table 2. Contact angles measured by Öner & McCarthy (2000, table 1) for water droplets exhibiting Fakir wetting on silane-modified hexagonally arrayed 40 μm high square posts, as a function of equilibrium contact angle. The parameters shown are averages of data from poles of three different widths (having the highest aspect ratios), and the equilibrium contact angles (θ_e) were calculated from the average of the flat surface advancing and receding angles. For all cases, $\phi = 0.25$.

purely thermodynamic processes that tend to an equilibrium state by dissipating energy to the surrounding environment. It is reassuring that thermodynamics predicts the same 'equilibrium' Cassie–Baxter angle for Fakir wetting as predicted by the present energy conservation method, under the assumption of zero 'stick–slip' dissipation (Shardt & Elliott 2020).

Another controversy in the field relates to whether area fractions (and indeed, surface properties) under entire droplets, or just in the locality of the TPCL, should be used to calculate CAH (Extrand 2003; Gao & McCarthy 2007*a*,*b*; McHale 2007; Nosonovsky 2007; Panchagnula & Vedantam 2007; Marmur 2022). Our analysis shows that CAH can be explained by energy conservation around the TPCL, rather than being a property of the surrounding flow system, and that the relevant area fractions used in the analysis (i.e. $A_{2C,ij}$ and $A_{1C,ij}$) represent those of the compound surfaces as they are advected into and out of the TPCL region. It is interesting that a group of publications has attempted to explain CAH by proposing modified local area fractions to use in the Cassie–Baxter equation that purportedly measure differential or contact-line-averaged roughness (McHale 2007; Choi *et al.* 2009; Erbil & Cansoy 2009; Raj *et al.* 2012; Xu 2016). Another group of publications contends that the observed contact-angle results from linear averaging of local contact angles existing along the TPCL (Extrand 2002). The present analysis does not support either of these concepts, instead showing that CAH has its origins in energy dissipation rather than simply a redefinition of ϕ or averaging of local angles.

We have applied our theory in a quantitative sense to the Fakir wetting state (see § 4.2.4). Equations (4.11*a*,*b*) show that the advancing and receding angles during Fakir wetting are related to the Cassie–Baxter angle by the dissipation that occurs during each of the movement stages, and consequently that the total dissipation that occurs around an advance and recede cycle (D_t) is composed of both the advance- and recede-stage dissipations. This observation is in contrast to some previous studies that assume that dissipation during advance is negligible (Reyssat & Quéré 2009; Butt *et al.* 2017). Notably, our theory applied to experimental data shows that the dissipation occurring during the advance stage is generally a very significant contribution to the total dissipation (from 73 % to 83 % in table 2). Confusingly, some previous studies also suggest that the advancing angle of a Fakir droplet is always 180°, and that measurement error is the cause of deviation from this value (Schellenberger *et al.* 2016). In reality, the dissipation during advance is actually at a maximum when $\theta_a = 180°$, and while we acknowledge the difficulties of measuring high advancing contact angles, a Fakir advancing angle that is less than 180° is consistent with theory and has been observed by multiple researchers.

The total dissipation D_t that occurs over an advance and recede cycle is an important parameter as it determines the mobility of the TPCL, or equivalently, the mobility of

a droplet. To reduce this total dissipation during Fakir wetting equation (4.12) shows that D_a can be minimised by using the lowest possible ϕ that still ensures Fakir stability – that is, the droplet remains tethered to the post ridges, and no interface touches the base of the structure – and by using a liquid, solid and structure combination that gives $\beta - \cos\theta_e$ closest to zero. In practice, biologically inspired super-hydrophobic surfaces use hierarchical roughness to provide effectively large θ_e at each length scale (matching $\beta \approx 1$), noting that flat-surface contact angles have a maximum of approximately 120° for chemically homogeneous and inert surfaces. The value of D_t can also be decreased by decreasing D_r, which also decreases with ϕ as described by (4.13), but is also proportional to the geometry-dependent parameter α.

Using the present theory applied to Fakir wetting, predictions of CAH can be made by choosing suitable values of the dissipation geometrical parameters α and β. Interestingly, β, which is concerned with the destruction of fluid/fluid interfaces during the advance event, appears to be approximately 1 for staggered arrays of roughness structures, but approximately 0.7 for roughness structures arranged in regular arrays. This suggests that less interface 'slip' motion occurs during the advance dissipation event in the latter case (see supplementary material, '1. Additional Fakir wetting data'). As shown in table 1 in the supplementary material, α, which is concerned with the destruction of fluid/fluid interfaces during the recede event, seems to be lower for staggered arrays as opposed to regular arrays, and lower for less complex pole cross-sections such as squares/circles as opposed to stars/crosses/diamonds, with both presumably related to the way the fluid/fluid interface deforms about the roughness structures during the liquid release. It is conceivable that α could be also influenced by very local topology effects due to (e.g.) manufacturing roughness/tolerances. However, for staggered arrays of circular poles, the data are reasonably well described by $\alpha \approx 0.3$, while $\alpha \approx 1$ for the examined regular arrays. As discussed in the supplementary material, the correlations of Jiang *et al.* (2019) and Reyssat & Quéré (2009) do not adequately describe the recede dissipations.

Equations that are similar in form to (4.1) have been used previously to describe roughness-induced CAH; however, the terminology or mechanism represented by the dissipation term varies (e.g. Priest *et al.* 2009; Reyssat & Quéré 2009; Ramiasa *et al.* 2013; Butt *et al.* 2017; Zhu & Dai 2019; Iliev, Pesheva & Iliev 2023). In summarising their experimental results (see the supplementary material), Priest *et al.* (2009) use an equivalent D_t defined as ϕ times a 'pinning energy' that is mathematically consistent with our Fakir model. Others refer to the equivalent D_t as a roughness-induced 'work of adhesion'; however, its precise definition varies. Butt *et al.* (2017), for example, calculated this work term as the amount of energy required to stretch the fluid/fluid interface away from the top of a pole during a recede motion. This is similar to, but not equivalent to, the dissipation derived in our analysis, in that it compares the energy state of the fluid/fluid interface before and after stretching (but in both cases still 'attached' to the solid), whereas the present dissipation term compares total surface energy between when the interface is stretched and after it depins and assumes an equilibrium shape. As reported, the Butt *et al.* (2017) analysis found 'work of adhesion' terms that were 2–3 times larger than that required to describe the Öner & McCarthy (2000) or Bico, Marzolin & Quéré (1999) regular pole data, despite also neglecting any contribution to CAH from the advance motion. (Additionally, as shown in table 2, for these particular datasets, the dissipation that occurs during receding is actually a much smaller contribution to the total dissipation than that occurring during the advance.) Reyssat & Quéré (2009) used a similar conceptual model for modelling their Fakir data. Zhu & Dai (2019) proposed that the total dissipation

is proportional to the intrinsic CAH; however, this concept is not supported by the data shown in the supplementary material. A major advance of the present study is that D_t, D_a and D_r are all defined unambiguously.

Other studies have proposed a completely new 'friction tension' term to explain CAH that again is used directly in place of the total dissipation term (Makkonen 2017). This tension is hypothesised to resist interface movement, and have a value equal to the energy of whatever surface is being formed. However, application of the theory on even a perfectly smooth and chemical homogeneous/inert surface leads to CAH values that have $\cos\theta_r - \cos\theta_a \approx 0.5$, equating to a CAH of approximately 30° for intermediate wetting systems. Smaller CAH for such surfaces can be achieved, however, largely invalidating this theory (Extrand 1998; e.g. 3° for water on octadecyltrichlorosilane). As discussed previously, line tension has been neglected in this study; however, if it were to be included, then the relevant D would be augmented with a $k/(h_{surround}\,\sigma_{12})$ term, where k is the line tension (in N) (Gaydos & Neumann 1987). For this term to be significant for millimetre size droplets requires k to be $O(10^{-4})$ N; however, experimental or theoretical estimates put this parameter in the range 10^{-9}–10^{-6} N or 10^{-10} N (Amirfazli & Neumann 2004), respectively, supporting the neglect of this force, at least at this length scale. Huang (2020) uses a similar 'string' tension concept to explain CAH. Note that as discussed previously, we have used the present theory combined with dynamic interface simulations (Kumar & Harvie 2024) to predict homogeneous wetting CAH ranges, finding excellent agreement with experimental results without the use of any friction, line or string tension concepts.

Finally, and as also discussed in the Introduction, some studies contend that contact-line distortion is the primary origin of roughness-induced CAH (Pomeau & Vannimenus 1985; Robbins & Joanny 1987; Öpik 2000; Raj *et al.* 2012). However, from the present analysis, distortion of the contact line, without the subsequent 'stick–slip' behaviour caused by strong defects (Joanny & de Gennes 1984), does not cause CAH (at least under our assumption of molecularly reversible interface creation). Distortion of the contact line is captured in the present mechanical energy balance via the surface potential contained in T_0 (see (3.11) and (3.12)), which ends up being $O(h_{rough}/X_{cv})$ smaller than the dominant terms (third term on the left-hand side of (3.26)) and so is not significant. Distortion of the contact line is, however, required to produce the 'stick–slip' motion required for energy dissipation, explaining why both proposed mechanisms share this observable trait.

5. Conclusion

Starting from a statement of momentum conservation, a mechanical energy conservation framework has been derived that allows the contact-angle hysteresis (CAH) range to be predicted from knowledge of the interfacial dynamics that occurs around an advancing three-phase contact line (TPCL). Unlike most previous works, the analysis is not specific to a particular wetting regime (e.g. Cassie or Wenzel) or particular surface structure (e.g. holes, poles, periodic, dilute). As a demonstration application, we have applied the theory to analyse the Fakir wetting regime using a model of how surface areas change during the advancing and receding 'stick–slip' dissipation events.

The analysis resolves a number of questions about wetting on rough surfaces that have been the source of confusion in the literature. We show:

(i) how energy conservation can be applied to the advancing TPCL for any roughness-induced wetting situation;

(ii) that the Wenzel and Cassie–Baxter angles are contained within the relevant CAH ranges, provided that the whole advance and recede motion is reversible, and that the wetting behaviour remains in the respective ranges;
(iii) how energy dissipation occurring during the advance of a Fakir interface is significant, and often larger than that occurring during the recede;
(iv) that contact-line distortion will not produce CAH in the absence of 'stick–slip' energy dissipation events.

Many limitations of the framework have been discussed and could form the basis of future extensions, including considering compressible, evaporating or dissolving fluids, irreversible work associated with interface creation or destruction, solid chemical heterogeneity, soft solids, and non-negligible CV advance speeds. In companion papers, the presented theory has been used successfully as a basis of numerical simulations to predict Wenzel wetting CAH on periodic surfaces (Kumar & Harvie 2024), to develop a correlation for the energy dissipation occurring during the Wenzel wetting of randomly structured surfaces (Kumar *et al.* 2024), and to demarcate the limits of Wenzel wetting by identifying alternative wetting regimes (Kumar *et al.* 2024).

6. Nomenclature

Arabic

A_{ij}	area of ij interface type
$A_{2C,ij}$	area of ij interface type entering CV as part of compound solid and phase ② interface
$A_{1C,ij}$	area of ij interface type leaving CV as part of compound solid and phase ① interface
A_{cv}	projected area of solid surface swept by CV over advance duration
$\widehat{\Delta A_{ij}}_k$	change in interfacial area ij during dissipation period k
Ca	roughness-scale capillary number ($v_{cap}\mu/\sigma$)
D	total energy dissipation occurring during advance
$\boldsymbol{e}_k$	coordinate unit vector in direction k
$\boldsymbol{g}$	gravity vector
h_{rough}	length scale of solid surface roughness
$h_{rough,crit}$	length scale of solid surface roughness that delimits viscous and inertial fluid flow regimes
$h_{surround}$	length scale of surrounding flow
h_{mol}	length scale of molecular or non-continuum effects within the fluid
$\boldsymbol{I}$	identity tensor
l_{cv}	length of CV
$\boldsymbol{n}_{cv}$	outward normal to surface of CV
$\boldsymbol{n}_{S,ij}$	unit normal vector of ij interface type, directed into phase i
m	number of material phases present within CV
p	pressure
p_0	reference pressure
$\hat{p}$	pressure within the fluid during a dissipation period
$\tilde{p}$	pressure within the fluid during an equilibrium period
r_{cv}	radius of CV
r_{cap}	distance to centre of dissipation event
$r_{cv,grav}$	capillary length
Re	roughness-scale Reynolds number ($\rho v_{cap}\, h_{rough}/\mu$)
S_{cv}	surface of CV
$S_{cv,cir}$	circumferential surface of CV

$S_{cv,end}$	end surface of CV
$S_{cv,br}$	circumferential surface of CV at the bottom right containing compound solid interfaces
$S_{cv,bl}$	circumferential surface of CV at the bottom left containing compound solid interfaces
$S_{cv,top}$	circumferential surface of CV at the top containing interface type 12
$S_{cv,fluid}$	surface of CV within fluid phases
t	time
$\hat{t}_k$	start of dissipation period k
$\tilde{t}_k$	start of equilibrium period k
$\widehat{\Delta t}_k$	duration of dissipation period k
$\widetilde{\Delta t}_k$	duration of equilibrium period k
$\bar{T}_i$	energy term i corresponding to total analysis period
$\hat{T}_{i,k}$	energy term i corresponding to dissipation period k
$\tilde{T}_{i,k}$	energy term i corresponding to equilibrium period k
V	volume
V_{cv}	volume of CV
$V_{cv,fluid}$	volume of CV containing fluid phases
$\overleftarrow{V}$	volume swept by $S_{cv,bl}$ over advance duration
$\overrightarrow{V}$	volume swept by $S_{cv,br}$ over advance duration
$\boldsymbol{v}$	velocity
v_{cap}	speed of fluid movement during dissipation events
v_{cv}	speed of CV advance
$\boldsymbol{v}_{cv}$	velocity of CV advance
$\tilde{\boldsymbol{v}}$	velocity of fluids during equilibrium periods
$\hat{\boldsymbol{v}}$	velocity of fluids during dissipation periods
$\widetilde{\boldsymbol{\nabla v}}$	velocity gradient within fluids during equilibrium periods
$\widehat{\boldsymbol{\nabla v}}$	velocity gradient within fluids during dissipation periods
We	roughness-scale Weber number ($\rho v_{cap}^2 h_{rough}/\sigma$)
X_{cv}	distance travelled by CV during total analysis period
x_{cv}	distance from start of CV travel
$\boldsymbol{x}_{cap}$	location of dissipation event
$\boldsymbol{x}_{s,ij}$	location of ij interface type

Greek

δ	one-dimensional Dirac delta function
$\delta_{S,ij}$	surface delta function for ij interface type
$\widehat{\Delta\sigma}$	sum of change in surface energies occurring over all dissipation events
μ	viscosity
$\hat{\Phi}$	gravitational potential function
ρ	density
σ	energy per unit area (interfacial tension)
σ_{ij}	energy per unit area (interfacial tension) of ij interface (between phases i and j)
σ_{2C}	compound energy per unit area of solid surface entering the CV from the right and under phase ②
σ_{1C}	compound energy per unit area of solid surface leaving the CV on the left and under phase ①
$\sum_{i<j}$	sum taken over all interface types ($= \sum_{j=1} \sum_{i=1}^{j-1}$)
T_M	material stress tensor
T_S	interfacial stress tensor
τ_{cap}	total duration of dissipation events occurring during CV advance
θ_a	macroscopic advancing angle of phase ① in phase ②
θ_r	macroscopic receding angle of phase ① in phase ②
θ_e	equilibrium angle of phase ① in phase ②

Supplementary material. Supplementary material is available at https://doi.org/10.1017/jfm.2024.317.

Acknowledgements. An early version of the work was presented at the 82nd ACS Colloid and Surface Science Symposium (Harvie *et al.* 2008). The author acknowledges conversations and collaborations with many people over this time frame regarding the application of this theory, including with Professor F. Grieser, Professor X. Zhang, Associate Professor B. Stadler, Professor W. Ducker, Professor D. Dunstan, Professor P. Mulvaney, Dr A. Haebich, Dr S. Mettu, Associate Professor H. Zhao, Dr P. Kumar and Professor S. Chakraborty. Dr P. Kumar completed a PhD at the University of Melbourne on the application of this theory, supported by a Melbourne–India postgraduate programme scholarship.

Funding. The majority of this theory was developed in 2007 while the author was between employment contracts. The work formed the basis for several unsuccessful Australian Research Council Discovery Project applications between the years 2008 and 2017 (DP0881399, DP0988840, DP150104699, DP160103697 and DP170104610). The author gratefully acknowledges the support of a Melbourne Institute of Materials Interdisciplinary Seed-Funding Scheme from the University of Melbourne in 2010 that was used to generate experimental results to support this theory.

Declaration of interests. The author reports no conflict of interest.

Author ORCIDs.
Dalton J.E. Harvie https://orcid.org/0000-0002-8501-1344.

Appendix A. Properties of the surface delta function (δ_S)

In this appendix, we derive three properties of the surface delta function that are used in § 2 in the derivation of the MMEB.

A.1. *Volume integral of the surface delta function*

We start with some definitions: for an interface that lies between a specific combination of immiscible materials, the surface delta function is given by Lafaurie *et al.* (1994)

$$\delta_S(\boldsymbol{x}) = \delta(q_1), \tag{A1}$$

where q_1 is the distance between $\boldsymbol{x}$ and the closest point on the interface surface, and δ is the one-dimensional Dirac delta function. As $\delta = 0$ when $q_1 \neq 0$, (A1) shows that δ_S is non-zero only on the interface surface.

For the analysis that follows, we require a more specific relationship between $\boldsymbol{x}$ and q_1 that is consistent with (A1): given that $q_1 = 0$ defines the interface surface, we specify the location of any point $\boldsymbol{x}$ that is near the surface via a series of coordinates $\boldsymbol{q} = (q_1, q_2, q_3)$ such that

$$\boldsymbol{x}(\boldsymbol{q}) = \boldsymbol{x}_S(q_2, q_3) + q_1\, \boldsymbol{n}_S(q_2, q_3). \tag{A2}$$

Here, q_2 and q_3 are a pair of convected surface coordinates (Aris 1962) that uniquely locate a material particle at $\boldsymbol{x}_S$ that lies on the interface surface, and $\boldsymbol{n}_S$ is a unit normal to the surface at $\boldsymbol{x}_S$ that is (consistently) directed into one of the phases. As $\boldsymbol{x}_S$ moves with the material, when q_2 and q_3 are held constant, we have

$$\frac{\mathrm{d}\boldsymbol{x}_S}{\mathrm{d}t} = \boldsymbol{v}, \tag{A3}$$

where $\boldsymbol{v}$ is the local material velocity.

Lines of constant q_2 and q_3 define the surface coordinate lines. As the surface coordinates move with the material, the coordinate lines will not in general be orthogonal to each other, even if they are initially. Provided that all material strain rates remain finite, however, they will not become coincident. This is important as it means that provided $\boldsymbol{x}_S$ can be defined uniquely in terms of q_2 and q_3 at some particular time, a unique relationship

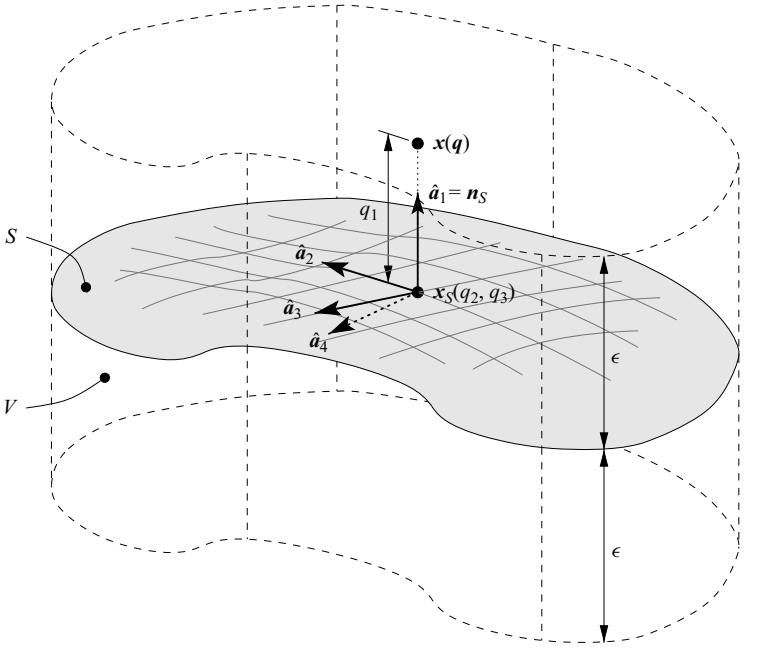

Figure 6. The smooth interface surface S separates two immiscible materials within a volume V. Expressed in terms of the convected surface coordinates (q_2, q_3), S is constant for all time.

between $\boldsymbol{x}_S$ and (q_2, q_3) will be realisable for all time (on a smooth and continuous surface).

To derive (2.3) and (2.7), we utilise a volume V that contains two immiscible materials that are separated by such a single smooth and continuous interface – surface S (see figure 6). The surface completely spans V such that the circumference of S occurs along the boundary of V. As the velocity within S is equal to that of the material (by (A3)), the boundary location of S is constant for all time when expressed in terms of the convected surface coordinates q_2 and q_3. Formally, V is constructed by projecting both above and below S in the direction of $\boldsymbol{n}_s$ a distance ϵ. Hence within V, $-\epsilon < q_1 < \epsilon$, and provided that ϵ is small enough, the relationship between $\boldsymbol{x}$ and $\boldsymbol{q}$ expressed by (A2) will be unique.

To derive (2.3), we integrate the surface delta function over V and express the integral in terms of the new coordinate system $\boldsymbol{q}$:

$$\int_V \delta_S(\boldsymbol{x})\,\mathrm{d}\boldsymbol{x} = \int_V \delta(q_1)\left[\frac{\partial \boldsymbol{x}}{\partial q_1}\cdot\left(\frac{\partial \boldsymbol{x}}{\partial q_2}\times\frac{\partial \boldsymbol{x}}{\partial q_3}\right)\right]\mathrm{d}\boldsymbol{q}. \tag{A4}$$

As the Dirac delta function $\delta(q_1)$ is non-zero only for $q_1 = 0$, the Jacobian in this equation (the term in square brackets) need be evaluated only for $q_1 = 0$. Hence, utilising (A2) to evaluate the partial derivatives, (A4) becomes

$$\int_V \delta_S(\boldsymbol{x})\,\mathrm{d}\boldsymbol{x} = \int_{-\epsilon}^{\epsilon} \delta(q_1)\,\mathrm{d}q_1 \int_S \boldsymbol{n}_S\cdot(\boldsymbol{a}_2\times\boldsymbol{a}_3)\,\mathrm{d}q_2\,\mathrm{d}q_3, \tag{A5}$$

where

$$\boldsymbol{a}_2 = \left.\frac{\partial \boldsymbol{x}}{\partial q_2}\right|_{q_1=0} = \frac{\partial \boldsymbol{x}_S}{\partial q_2} \quad \text{and} \quad \boldsymbol{a}_3 = \left.\frac{\partial \boldsymbol{x}}{\partial q_3}\right|_{q_1=0} = \frac{\partial \boldsymbol{x}_S}{\partial q_3} \tag{A6a,b}$$

are two non-coincident vectors that are tangential to S at $\boldsymbol{x}_S$. By definition of the Dirac delta function, the first integral on the right-hand side of (A5) is equal to 1 (as ϵ is a small positive number). For the second integral, we note that the vectors $\boldsymbol{a}_2$ and $\boldsymbol{a}_3$ are both orthogonal to $\boldsymbol{n}_S$, hence without loss of generality, we define

$$\boldsymbol{n}_S = \frac{\boldsymbol{a}_2 \times \boldsymbol{a}_3}{|\boldsymbol{a}_2 \times \boldsymbol{a}_3|}. \tag{A7}$$

This allows the volume integral of δ_S to be written as

$$\int_V \delta_S(\boldsymbol{x})\,\mathrm{d}\boldsymbol{x} = \int_S \left|\frac{\partial \boldsymbol{x}_S}{\partial q_2} \times \frac{\partial \boldsymbol{x}_S}{\partial q_3}\right| \mathrm{d}q_2\,\mathrm{d}q_3 = \int_S \mathrm{d}S = A, \tag{A8}$$

where A is the area of surface S (Kreyszig 2006, p. 454, § 10.6). Noting that any volume containing arbitrary surfaces can be composed of volumes that contain smooth and continuous surfaces and volumes that contain no surface (in which (A8) is trivially satisfied), (2.3) from the main text results.

A.2. *Surface delta function transport equation*

To derive (2.7), we take the derivative of (A8) with respect to time. Recognising that the boundary location of S is constant in terms of q_2 and q_3, the time derivative commutes into the integral, giving

$$\frac{\mathrm{d}}{\mathrm{d}t}\int_V \delta_S(\boldsymbol{x})\,\mathrm{d}\boldsymbol{x} = \int_S \frac{\mathrm{d}}{\mathrm{d}t}[|\boldsymbol{a}_2 \times \boldsymbol{a}_3|]\,\mathrm{d}q_2\,\mathrm{d}q_3. \tag{A9}$$

Performing the differentiation and (re)introducing the Dirac delta function leads to

$$\begin{aligned}\frac{\mathrm{d}}{\mathrm{d}t}\int_V \delta_S(\boldsymbol{x})\,\mathrm{d}\boldsymbol{x} &= \int_{-\epsilon}^{\epsilon} \delta(q_1)\,\mathrm{d}q_1 \int_S \mathcal{A}(\boldsymbol{q})\,|\boldsymbol{a}_2 \times \boldsymbol{a}_3|\,\mathrm{d}q_2\,\mathrm{d}q_3 \qquad (A10)\\ &= \int_V \delta(q_1)\,\mathcal{A}(\boldsymbol{q})\left[\frac{\partial \boldsymbol{x}}{\partial q_1}\cdot\left(\frac{\partial \boldsymbol{x}}{\partial q_2}\times\frac{\partial \boldsymbol{x}}{\partial q_3}\right)\right]\mathrm{d}\boldsymbol{q}\\ &= \int_V \delta_S(\boldsymbol{x})\,\mathcal{A}(\boldsymbol{x})\,\mathrm{d}\boldsymbol{x}, \qquad (A11)\end{aligned}$$

where

$$\mathcal{A} = \frac{\boldsymbol{a}_2 \times \boldsymbol{a}_3}{|\boldsymbol{a}_2 \times \boldsymbol{a}_3|^2}\cdot\left[\frac{\mathrm{d}\boldsymbol{a}_2}{\mathrm{d}t}\times\boldsymbol{a}_3 + \boldsymbol{a}_2 \times \frac{\mathrm{d}\boldsymbol{a}_3}{\mathrm{d}t}\right] \tag{A12}$$

is a function of the local surface geometry.

To simplify the expression for $\mathcal{A}$, we recall from (A5) that the surface integral in (A10) that contains $\mathcal{A}$ is evaluated under the condition $q_1 = 0$. Assuming this condition, we combine (A3) and (A6*a*,*b*) to derive the identity

$$\begin{aligned}\frac{\mathrm{d}\boldsymbol{a}_2}{\mathrm{d}t} &= \frac{\mathrm{d}}{\mathrm{d}t}\left(\frac{\partial \boldsymbol{x}_S}{\partial q_2}\right) = \frac{\partial}{\partial q_2}\left(\frac{\mathrm{d}\boldsymbol{x}_S}{\mathrm{d}t}\right) = \frac{\partial \boldsymbol{v}}{\partial q_2} = \frac{\partial \boldsymbol{x}}{\partial q_2}\cdot\nabla\boldsymbol{v}\\ &= \frac{\partial \boldsymbol{x}_S}{\partial q_2}\cdot\nabla\boldsymbol{v} = \boldsymbol{a}_2\cdot\nabla\boldsymbol{v}. \qquad (A13)\end{aligned}$$

Substituting this and an analogous result for $\mathrm{d}\boldsymbol{a}_3/\mathrm{d}t$ into (A12) yields

$$\mathcal{A} = \beta^2(\hat{\boldsymbol{a}}_2 \times \hat{\boldsymbol{a}}_3) \cdot [(\hat{\boldsymbol{a}}_2 \cdot \boldsymbol{\nabla}\boldsymbol{v}) \times \hat{\boldsymbol{a}}_3 + \hat{\boldsymbol{a}}_2 \times (\hat{\boldsymbol{a}}_3 \cdot \boldsymbol{\nabla}\boldsymbol{v})], \tag{A14}$$

where

$$\hat{\boldsymbol{a}}_2 = \frac{\boldsymbol{a}_2}{|\boldsymbol{a}_2|} \quad \text{and} \quad \hat{\boldsymbol{a}}_3 = \frac{\boldsymbol{a}_3}{|\boldsymbol{a}_3|} \tag{A15a,b}$$

are unit vectors in each of the two surface coordinate directions, and $\beta = |\hat{\boldsymbol{a}}_2 \times \hat{\boldsymbol{a}}_3|^{-1}$.

We now define a fourth unit vector $\hat{\boldsymbol{a}}_4$ that is coplanar with $\hat{\boldsymbol{a}}_2$ and $\hat{\boldsymbol{a}}_3$ (and hence tangential to S) such that the vectors $(\boldsymbol{n}_S, \hat{\boldsymbol{a}}_2, \hat{\boldsymbol{a}}_4)$ form a right-handed coordinate system at $\boldsymbol{x}_S$ (as shown in figure 6). As the orientation of $\hat{\boldsymbol{a}}_4$ obeys $\boldsymbol{n}_S = \hat{\boldsymbol{a}}_2 \times \hat{\boldsymbol{a}}_4$, the new vector can be expressed as

$$\hat{\boldsymbol{a}}_4 = \alpha\hat{\boldsymbol{a}}_2 + \beta\hat{\boldsymbol{a}}_3, \quad \text{or} \quad \hat{\boldsymbol{a}}_3 = \frac{1}{\beta}(\hat{\boldsymbol{a}}_4 - \alpha\hat{\boldsymbol{a}}_2), \tag{A16a,b}$$

where α is a finite scalar, and (A7) has been used. Substituting (A15*a*,*b*) into (A14) yields, after some simplification,

$$\mathcal{A} = (\hat{\boldsymbol{a}}_2 \times \hat{\boldsymbol{a}}_4) \cdot [(\hat{\boldsymbol{a}}_2 \cdot \boldsymbol{\nabla}\boldsymbol{v}) \times \hat{\boldsymbol{a}}_4 + \hat{\boldsymbol{a}}_2 \times (\hat{\boldsymbol{a}}_4 \cdot \boldsymbol{\nabla}\boldsymbol{v})]. \tag{A17}$$

Employing the identity (Bird *et al.* 2002, p. 814, § A.2)

$$[\boldsymbol{u} \times \boldsymbol{v}] \cdot [\boldsymbol{w} \times \boldsymbol{z}] = (\boldsymbol{u} \cdot \boldsymbol{w})(\boldsymbol{v} \cdot \boldsymbol{z}) - (\boldsymbol{u} \cdot \boldsymbol{z})(\boldsymbol{v} \cdot \boldsymbol{w}), \tag{A18}$$

and noting that $\hat{\boldsymbol{a}}_2 \cdot \hat{\boldsymbol{a}}_4 = 0$, leads to

$$\mathcal{A} = \hat{\boldsymbol{a}}_2\hat{\boldsymbol{a}}_2 : \boldsymbol{\nabla}\boldsymbol{v} + \hat{\boldsymbol{a}}_4\hat{\boldsymbol{a}}_4 : \boldsymbol{\nabla}\boldsymbol{v} = (\boldsymbol{I} - \boldsymbol{n}_S\boldsymbol{n}_S) : \boldsymbol{\nabla}\boldsymbol{v}, \tag{A19}$$

where $\boldsymbol{I}$ is the unit tensor.

With $\mathcal{A}$ defined, we return to the development of (A11). Noting that for $\delta_S \neq 0$, the boundary of V moves at the local material velocity $\boldsymbol{v}$, the left-hand side of this equation can be expanded using the Leibniz formula for differentiating a volume integral and the Gauss–Ostrogradskii divergence theorem. On the right-hand side we substitute $\mathcal{A}$ from (A19). These operations yield

$$\int_V \frac{\partial \delta_S}{\partial t}\,\mathrm{d}\boldsymbol{x} + \int_V \boldsymbol{\nabla} \cdot (\delta_S \boldsymbol{v})\,\mathrm{d}\boldsymbol{x} = \int_V \delta_S(\boldsymbol{I} - \boldsymbol{n}_S\boldsymbol{n}_S) : \boldsymbol{\nabla}\boldsymbol{v}\,\mathrm{d}\boldsymbol{x}. \tag{A20}$$

Equation (A20) is valid for a specific volume geometry that contains a single smooth and continuous interface surface. However, (A20), like (A8), is trivially satisfied in volumes that contain no interface surface. As any volume can be composed of volumes that contain a smooth and continuous interface surface, and volumes that contain no interface surface, (A20) must hold for any arbitrary volume. Hence (A20) must hold at all locations and (2.7) from the main text results.

A.3. *Surface integral of the surface delta function*

In order to apply the mechanical energy balance of (2.10), we also need to be able to evaluate the integral of the surface delta function over a surface. In the following, we derive (2.4) that is given in the main text for this purpose.

The derivation is based on a small amount of interfacial area, ΔA, that has a length of Δl, and that is contained within a small element of volume ΔV. The volume element is

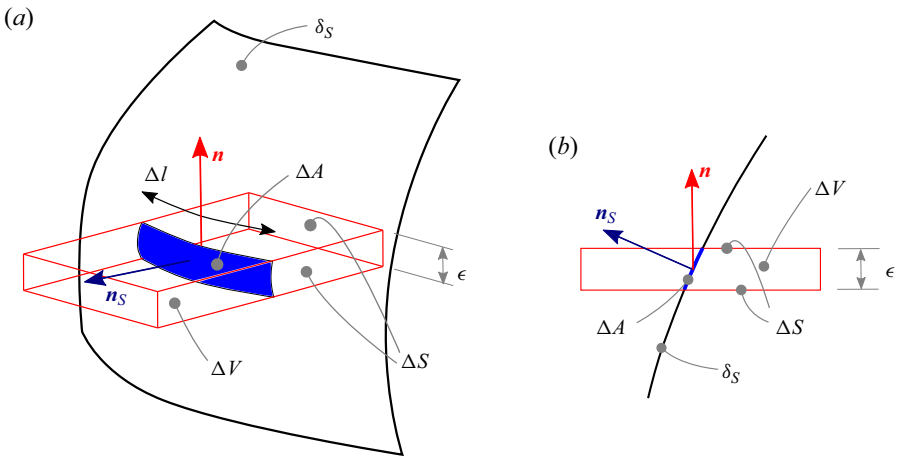

Figure 7. The two-dimensional integral of the delta function.

thin in the direction of $\boldsymbol{n}$, having a thickness of ϵ in this direction, so that $\Delta V = \epsilon\,\Delta S$, where ΔS is a small part of a larger surface S. Figures 7(*a*,*b*) describe this geometrical system using a projection and cross-section, respectively.

The starting point for the analysis is the definition of the surface delta function, i.e. (2.3), applied to the small volume ΔV. This gives

$$\Delta A = \int_{\Delta V} \delta_S \,\mathrm{d}V = \int_{-\epsilon/2}^{\epsilon/2} \int_{\Delta S} \delta_S \,\mathrm{d}S \,\mathrm{d}x_{\boldsymbol{n}} \approx \epsilon \int_{\Delta S} \delta_S \,\mathrm{d}S, \tag{A21}$$

where $x_{\boldsymbol{n}}$ is a coordinate in the direction of $\boldsymbol{n}$ centred on ΔA. The last equality holds true for small ϵ. Meanwhile, for small ΔA, $\boldsymbol{n}_S$ is approximately uniform over ΔA, and the geometry of the intersecting surfaces gives (see figure 7*b*)

$$\Delta A = \frac{\Delta l\,\epsilon}{\sqrt{1-(\boldsymbol{n}_S\cdot\boldsymbol{n})^2}}. \tag{A22}$$

Equating (A21) and (A22) leads to

$$\int_{\Delta S} \delta_S \,\mathrm{d}S = \frac{\Delta l}{\sqrt{1-(\boldsymbol{n}_S\cdot\boldsymbol{n})^2}}. \tag{A23}$$

Finally, recognising that ΔS is a small section of a larger surface S, and that Δl is a small section of the entire intersection between S and δ_S that has length l, (A23) can be generalised in the limit $\Delta l \to 0$ to

$$\int_S \delta_S \,\mathrm{d}S = \int_0^l \frac{\mathrm{d}l'}{\sqrt{1-(\boldsymbol{n}_S\cdot\boldsymbol{n})^2}}, \tag{A24}$$

where l' is a path length parametrisation of the curve that is defined as the intersection between S and δ_S, and $\boldsymbol{n}_S\cdot\boldsymbol{n}$ is a function of l'. Equation (A24) is the most general form of this surface delta identity; however, by assuming that $\boldsymbol{n}_S\cdot\boldsymbol{n}$ is independent of the path length l', (2.4) from the main text results.

Appendix B. Examining each term in the contact-line energy balance

The objective in this appendix is to apply the physical system and material dynamics models defined in §§ 3.1 and 3.2 to each term in the contact-line energy balance of (3.25), finding either its analytical expression or order of magnitude.

B.1. *Examining term* $\bar{T}_0$

This term represents the change in mechanical energy within the CV between the start and end of the advance. Defining the notation $\overline{\Delta a} = a(t=\tau) - a(t=0)$, $\bar{T}_0$ can be expressed using (3.11) and (3.12) as

$$\begin{aligned}\bar{T}_0 &= \frac{1}{A_{cv}}\,\overline{\Delta E} \\ &= \frac{1}{A_{cv}}\int_{V_{cv}} \frac{1}{2}\,\overline{\Delta(\rho v^2)}\,\mathrm{d}V + \frac{1}{A_{cv}}\int_{V_{cv}} \overline{\Delta\rho}\,\hat{\Phi}\,\mathrm{d}V + \sum_{i<j}\frac{\sigma_{ij}\,\overline{\Delta A_{ij}}}{A_{cv}}.\end{aligned} \tag{B1}$$

The first term on the right-hand side of this equation captures changes to the kinetic energy within the CV between the start and end of the advance. As both $t=0$ and $t=\tau$ are within equilibrium periods, changes to ρv^2 within the CV between $t=0$ and τ will be limited to a fluid volume that is within $O(h_{rough})$ of the solid surface. Further, as fluid velocities are $O(v_{cv})$ at both times, the first term can be evaluated as $O(\rho v_{cv}^2\, h_{rough}\, r_{cv}/X_{cv})$ after cancelling l_{cv}. Similarly, for the second gravitational potential energy term, changes to ρ are also limited to the same volume within $O(h_{rough})$ of the solid. Recognising that the gravitational potential function satisfies $\hat{\Phi} = \boldsymbol{g}\cdot\boldsymbol{x}$, a maximum magnitude for this potential function within the CV is $\hat{\Phi} = O(g l_{cv})$, where $g = |\boldsymbol{g}|$ is the gravitational constant. Finally, for the third term in (B1), which represents the change in surface potential energy within the CV between the start and end of the advance, the change in area of each interface will be of $O(h_{rough}\, l_{cv})$, being composed of changes to interfacial areas that occur around the TPCL, as well as changes to the average of each A_{ij} associated with solid interfaces under each of the fluid phases due to the (possibly) random nature of the surface defects.

With these assumptions, the change in mechanical energy over the duration of the advance is evaluated as

$$\begin{aligned}\bar{T}_0 &= O\left(\frac{\rho v_{cv}^2 r_{cv}\, h_{rough}}{X_{cv}}\right) + O\left(\frac{\rho g r_{cv} l_{cv}\, h_{rough}}{X_{cv}}\right) + O\left(\frac{\sigma\, h_{rough}}{X_{cv}}\right) \\ &= O(\rho v_{cv}^2\, h_{rough}) + O(\rho g l_{cv}\, h_{rough}) + O\left(\frac{\sigma\, h_{rough}}{X_{cv}}\right),\end{aligned} \tag{B2}$$

where in the last line we have used $O(r_{cv}) = O(X_{cv})$.

B.2. *Examining term* $\sum_{k=1}^{N}\hat{T}_{0,k}$

In a similar fashion to $\bar{T}_0$, but here concerned with each dissipation period, $\hat{T}_{0,k}$ represents the change in mechanical energy within the CV occurring over the period of the kth dissipation event. Defining $\widehat{\Delta a}_k = a(t=\hat{t}_k + \widehat{\Delta t}_k) - a(t=\hat{t}_k)$, this change in energy can

be expressed as

$$\hat{T}_{0,k} = \frac{1}{A_{cv}} \widehat{\Delta E}_k = \frac{1}{A_{cv}} \int_{V_{cv}} \frac{1}{2} \widehat{\Delta(\rho v^2)}_k \, \mathrm{d}V + \frac{1}{A_{cv}} \int_{V_{cv}} \widehat{\Delta\rho}_k \, \hat{\Phi} \, \mathrm{d}V + \sum_{i<j} \frac{\sigma_{ij} \, \widehat{\Delta A}_{ijk}}{A_{cv}}, \tag{B3}$$

where $\widehat{\Delta A}_{ijk}$ is the change in area of interface ij that is contained within the CV and that occurs over the kth dissipation event.

In order to evaluate the magnitude of the terms appearing in (B3), we return to our conceptual model for how the fluid and interfaces behave during dissipation events. During a dissipation event, an area of the TPCL 'depins' from a particular surface defect and moves at a capillary-driven velocity to a new 'equilibrium' interface position. These dissipation events cause interfacial areas to change by $O(h_{rough}^2)$, and as interfacial curvatures resulting from the roughness extend by $O(h_{rough})$ into the fluid, cause fluid properties to change within a volume of $O(h_{rough}^3)$ near the TPCL. Hence changes to the kinetic energy and density within a volume of $O(h_{rough}^3)$ caused by each dissipation event will contribute to the first two terms on the right-hand side of (B3), while changes of $O(h_{rough}^2)$ to the interfacial areas of each phase combination due to each dissipation event will contribute to the third term on the right-hand side of this equation.

Concurrently, over the duration of each dissipation event ($\widehat{\Delta t}_k$), continuous movement of the TPCL still occurs across the rough surface, and this movement also contributes to the terms on the right-hand side of (B3). Specifically, within $O(h_{rough})$ of the TPCL, or a volume of $O(\widehat{\Delta t}_k \, v_{cv} l_{cv} \, h_{rough})$, there will be a change in kinetic energy and density of the fluid occurring due to the continuous TPCL movement that will add contributions to the first two terms on the right-hand side of (B3). Similarly, for the third term on the right-hand side of (B3), there will also be a change in interfacial areas of $O(\widehat{\Delta t}_k \, v_{cv} l_{cv})$ due to the continuous TPCL movement that also needs to be included.

Hence, summing changes due to both the specific dissipation event and continuous TPCL movement occurring during each dissipation period, the magnitude of $\hat{T}_{0,k}$ can be expressed as

$$\begin{aligned} \hat{T}_{0,k} = {} & O\left(\frac{\rho v_{cv}^2 \, h_{rough}^3}{X_{cv} l_{cv}}\right) + O\left(\frac{\rho v_{cv}^3 \, h_{rough} \, \widehat{\Delta t}_k}{X_{cv}}\right) \\ & + O\left(\frac{\rho g \, h_{rough}^4}{X_{cv} l_{cv}}\right) + O\left(\frac{\rho g l_{cv} v_{cv} \, h_{rough} \, \widehat{\Delta t}_k}{X_{cv}}\right) \\ & + O\left(\frac{\sigma \, h_{rough}^2}{X_{cv} l_{cv}}\right) + O\left(\frac{\sigma \, v_{cv} \, \widehat{\Delta t}_k}{X_{cv}}\right), \end{aligned} \tag{B4}$$

where the three pairs of terms correspond to the first, second and third terms appearing on the right-hand side of (B3), respectively, with the first of each pair corresponding to changes caused by the specific capillary-driven dissipation event, and the second corresponding to the changes due to continuous TPCL movement that occurs during each dissipation event period.

Returning to (3.25), it is actually the sum of $\hat{T}_{0,k}$ from all N dissipation events that is required in the contact-angle mechanical energy balance. Performing this sum on (B4), while noting $\sum_{k=1}^{N} \widehat{\Delta t}_k = \tau_{cap}$, $N = O(X_{cv} l_{cv}/h_{rough}^2)$ and $v_{cv}\tau = X_{cv}$, leads to

$$\begin{aligned}\sum_{k=1}^{N} \hat{T}_{0,k} = {} & O(\rho v_{cv}^2 h_{rough}) + O\left(\rho v_{cv}^2 h_{rough} \frac{\tau_{cap}}{\tau}\right) \\ & + O(\rho g h_{rough}^2) + O\left(\rho g l_{cv} h_{rough} \frac{\tau_{cap}}{\tau}\right) \\ & + O(\sigma) + O\left(\sigma \frac{\tau_{cap}}{\tau}\right).\end{aligned} \tag{B5}$$

Noting from (3.6) that $O(\tau_{cap}/\tau) \ll 1$, terms involving this ratio can be neglected in comparison to other terms, and recognising that the $O(\sigma)$ term in the above originated from the final term of (B3), we arrive at

$$\sum_{k=1}^{N} \hat{T}_{0,k} = O(\rho v_{cv}^2 h_{rough}) + O(\rho g h_{rough}^2) + \widehat{\Delta\sigma}. \tag{B6}$$

The specific dissipation event surface energy change per area traversed ($\widehat{\Delta\sigma}$) is defined using (3.31) in the main text.

The next six terms all correspond to energy transfers that occur during the equilibrium stages of the advance.

B.3. *Examining term* $\sum_{k=1}^{N+1} \tilde{T}_{1,k}$

This term represents transport of surface potential energy through the boundary of the CV during the equilibrium stages due only to movement of the CV. Introducing the shorthand notation $\int_{\widetilde{\Delta t}_k} \mathrm{d}t = \int_{\tilde{t}_k}^{\tilde{t}_k + \widetilde{\Delta t}_k} \mathrm{d}t$, applying (3.13) over $\widetilde{\Delta t}_k$ gives

$$\sum_{k=1}^{N+1} \tilde{T}_{1,k} = \frac{1}{A_{cv}} \sum_{k=1}^{N+1} \int_{\widetilde{\Delta t}_k} \int_{S_{cv}} \sum_{i<j} \sigma_{ij} \delta_{S,ij} \boldsymbol{n}_{cv} \cdot \boldsymbol{v}_{cv} \, \mathrm{d}S \, \mathrm{d}t. \tag{B7}$$

Further, noting that $\boldsymbol{n}_{cv} \cdot \boldsymbol{v}_{cv}$ on the ends of the CV ($S_{cv,end}$), and that σ_{ij} is non-zero only within three thin regions on the circumference of the CV ($S_{cv,cir}$) where the interfaces cross its boundary, (B7) can be written as the sum of three terms

$$\begin{aligned}\sum_{k=1}^{N+1} \tilde{T}_{1,k} = {} & \frac{1}{A_{cv}} \sum_{k=1}^{N+1} \int_{\widetilde{\Delta t}_k} \int_{S_{cv,top}} \sigma_{12} \delta_{S,12} \boldsymbol{n}_{cv} \cdot \boldsymbol{v}_{cv} \, \mathrm{d}S \, \mathrm{d}t \\ & + \frac{1}{A_{cv}} \sum_{k=1}^{N+1} \int_{\widetilde{\Delta t}_k} \int_{S_{cv,bl}} \sum_{i<j} \sigma_{ij} \delta_{S,ij} \boldsymbol{n}_{cv} \cdot \boldsymbol{v}_{cv} \, \mathrm{d}S \, \mathrm{d}t \\ & + \frac{1}{A_{cv}} \sum_{k=1}^{N+1} \int_{\widetilde{\Delta t}_k} \int_{S_{cv,br}} \sum_{i<j} \sigma_{ij} \delta_{S,ij} \boldsymbol{n}_{cv} \cdot \boldsymbol{v}_{cv} \, \mathrm{d}S \, \mathrm{d}t.\end{aligned} \tag{B8}$$

Here, as indicated in figure 8, $S_{cv,top}$, $S_{cv,bl}$ and $S_{cv,br}$ are the three thin regions mentioned above that just contain the fluid interface (top), interfaces associated with the solid surface

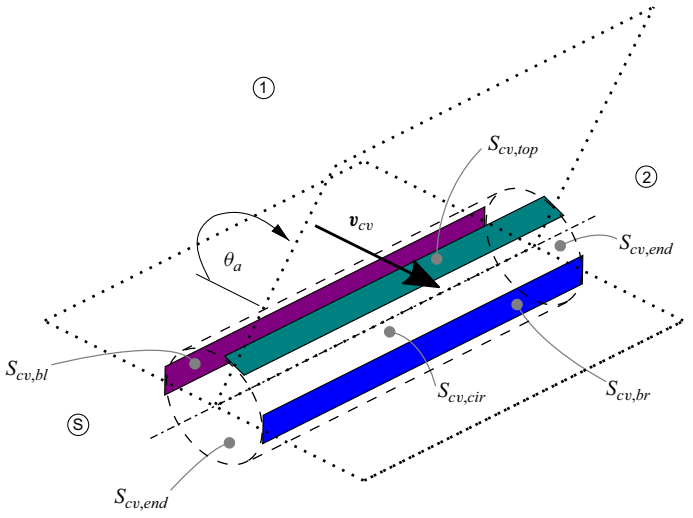

Figure 8. Three thin regions on the circumference of the CV ($S_{cv,cir}$) are defined that contain all of the phase interfaces that intersect with this boundary.

under phase ① (bl, bottom left) and interfaces associated with the solid surface under phase ② (br, bottom right), respectively.

For the first term on the right-hand side of (B8), as $\boldsymbol{n}_{cv} = -\cos\theta_a\,\boldsymbol{e}_1 + \sin\theta_a\,\boldsymbol{e}_3$ where the fluid interface crosses the CV boundary at $S_{cv,top}$, and as $\boldsymbol{v}_{cv} = v_{cv}\boldsymbol{e}_1$, $\boldsymbol{n}_{cv}\cdot\boldsymbol{v}_{cv} = -v_{cv}\cos\theta_a$ at this location. Further, following the interface description outlined in § 3.1, $\boldsymbol{n}_{cv}\cdot\boldsymbol{n}_{S,ij} = 0$ at this location at all times, and as $S_{cv,top}$ is infinitely thin in the circumferential direction at this location, (2.4) shows that $\int_{S_{cv,top}} \delta_{S,ij}\,\mathrm{d}S = l_{cv}$. Hence the first term on the right-hand side of (B8) becomes

$$\frac{1}{A_{cv}}\sum_{k=1}^{N+1}\int_{\widetilde{\Delta}t_k}\int_{S_{cv,top}} \sigma_{12}\delta_{S,ij}\boldsymbol{n}_{cv}\cdot\boldsymbol{v}_{cv}\,\mathrm{d}S\,\mathrm{d}t = -\frac{\sigma_{12}v_{cv}\cos\theta_a}{X_{cv}}\sum_{k=1}^{N+1}\widetilde{\Delta}t_k$$
$$= -\left(1-\frac{\tau_{cap}}{\tau}\right)\sigma_{12}\cos\theta_a. \qquad \text{(B9)}$$

The second and third terms on the right-hand side of (B8) represent the transport of surface potential energy associated with the rough solid surface out of, and into, respectively, the CV as it advances across the solid. Note that these surface energies may include contributions from micro-droplets or bubbles confined within the surface roughness, as well as from the surface energy between the solid and adjacent bulk fluid phase.

Focusing our explanation on the second term on the right-hand side of (B8), which involves an integral over $S_{cv,bl}$, we first note that as $S_{cv,bl}$ only has to include phase interfaces that are associated with the surface roughness, the circumferential height of $S_{cv,bl}$ is only of $O(h_{rough})$. Further, as $h_{rough} \ll r_{cv}$ (via (3.1)), we have $\boldsymbol{n}_{cv} = -\boldsymbol{e}_1$ at this location, and consequently $\boldsymbol{n}_{cv}\cdot\boldsymbol{v}_{cv} = -v_{cv}$. Splitting the temporal integration using (3.3) leads to

$$\frac{1}{A_{cv}}\sum_{k=1}^{N+1}\int_{\widetilde{\Delta}t_k}\int_{S_{cv,bl}}\sum_{i<j}\sigma_{ij}\delta_{S,ij}\boldsymbol{n}_{cv}\cdot\boldsymbol{v}_{cv}\,\mathrm{d}S\,\mathrm{d}t$$

$$= -\frac{v_{cv}}{X_{cv} l_{cv}} \sum_{i<j} \sigma_{ij} \int_0^{\tau} \int_{S_{cv,bl}} \delta_{S,ij} \, \mathrm{d}S \, \mathrm{d}t$$

$$- \frac{v_{cv}}{X_{cv} l_{cv}} \sum_{i<j} \sigma_{ij} \sum_{k=1}^{N+1} \int_{\widehat{\Delta t}_k} \int_{S_{cv,bl}} \delta_{S,ij} \, \mathrm{d}S \, \mathrm{d}t. \tag{B10}$$

For the first term on the right-hand side of this equation, we define a new volume $\overleftarrow{V}$ that is created by sweeping $S_{cv,bl}$ over the solid surface for the duration of the advance. Formally, we define a coordinate $x_{cv} = t v_{cv}$ that increases in the direction of $\boldsymbol{e}_1$ and measures the progress of the CV as it moves over the solid surface, giving

$$\begin{aligned} v_{cv} \sum_{i<j} \sigma_{ij} \int_0^{\tau} \int_{S_{cv,bl}} \delta_{S,ij} \, \mathrm{d}S \, \mathrm{d}t &= \sum_{i<j} \sigma_{ij} \int_0^{X_{cv}} \int_{S_{cv,bl}} \delta_{S,ij} \, \mathrm{d}S \, \mathrm{d}x_{cv} \\ &= \sum_{i<j} \sigma_{ij} \int_{\overleftarrow{V}} \delta_{S,ij} \, \mathrm{d}V \\ &= \sum_{i<j} \sigma_{ij} A_{1C,ij}, \end{aligned} \tag{B11}$$

where $A_{1C,ij}$ is the area of each interface type ij associated with the rough solid surface that leaves the CV during its advance over the solid.

For the second term on the right-hand side of (B10), we calculate its order of magnitude rather than deriving an expression, noting that $\sum_{k=1}^{N} \widehat{\Delta t}_k = \tau_{cap}$ and $\int_{S_{cv,bl}} \delta_{S,ij} \, \mathrm{d}S = O(l_{cv})$. Incorporating these expressions and (B11) back into (B10) gives

$$\frac{1}{A_{cv}} \sum_{k=1}^{N+1} \int_{\widetilde{\Delta t}_k} \int_{S_{cv,bl}} \sum_{i<j} \sigma_{ij} \delta_{S,ij} \boldsymbol{n}_{cv} \cdot \boldsymbol{v}_{cv} \, \mathrm{d}S \, \mathrm{d}t = -\sum_{i<j} \sigma_{ij} \frac{A_{1C,ij}}{A_{cv}} + O\left(\frac{\tau_{cap}}{\tau} \sigma\right), \tag{B12}$$

completing the evaluation of the second term on the right-hand side of (B8).

Finally, performing an analogous calculation for the third term on the right-hand side of (B8) for the solid surface interfaces $A_{2C,ij}$ that lie under phase ② and that enter the CV through $S_{cv,br}$ during the advance, and noting again as per (3.6) that terms involving the factor τ_{cap}/τ can be neglected relative to those that do not include this term, the surface potential energy transport term from (B8) can be written as

$$\sum_{k=1}^{N+1} \tilde{T}_{1,k} = -\sigma_{12} \cos\theta_a + \sigma_{2C} - \sigma_{1C}, \tag{B13}$$

where the compound surface energies associated with the solid interface that is leaving (σ_{1C}) and entering (σ_{2C}) the advancing CV are defined by (3.30) in the main text.

B.4. *Examining term* $\sum_{k=1}^{N+1} \tilde{T}_{2,k}$

This term represents the transport of kinetic energy into the CV during the equilibrium stages, and is given by

$$\sum_{k=1}^{N+1} \tilde{T}_{2,k} = \frac{1}{A_{cv}} \sum_{k=1}^{N+1} \int_{\widetilde{\Delta t}_k} \int_{S_{cv}} \boldsymbol{n}_{cv} \cdot \frac{1}{2} \rho v^2 (\boldsymbol{v}_{cv} - \boldsymbol{v}) \, \mathrm{d}S \, \mathrm{d}t. \tag{B14}$$

Noting from § 3.2 that velocities are zero within the solid phase and within the equilibrium stages within the fluid are $\tilde{\boldsymbol{v}} = O(v_{cv})$, and that the fluid areas of $S_{cv,cir}$ and $S_{cv,end}$ have areas of $O(r_{cv}l_{cv})$ and $O(r_{cv}^2)$, respectively, the magnitude of this term is given by

$$\sum_{k=1}^{N+1} \tilde{T}_{2,k} = O\left((\tau - \tau_{cap})\rho v_{cv}^3 \frac{r_{cv}^2 + l_{cv}r_{cv}}{X_{cv}l_{cv}}\right) = O(\rho v_{cv}^2 r_{cv}). \tag{B15}$$

In deriving the final term in this expression, we have used $O(l_{cv}) = O(r_{cv})$ and neglected a term containing τ_{cap}/τ relative to one that does not, consistent with (3.6).

B.5. *Examining term* $\sum_{k=1}^{N+1} \tilde{T}_{3,k}$

This term represents the transport of gravitational potential energy into the CV during the equilibrium stages, and is given by

$$\sum_{k=1}^{N+1} \tilde{T}_{3,k} = \frac{1}{A_{cv}} \sum_{k=1}^{N+1} \int_{\widetilde{\Delta t}_k} \int_{S_{cv}} \boldsymbol{n}_{cv} \cdot \rho\, \hat{\Phi}(\boldsymbol{v}_{cv} - \boldsymbol{v})\, \mathrm{d}S\, \mathrm{d}t. \tag{B16}$$

In a very similar fashion to the last term, this term has a magnitude given by

$$\sum_{k=1}^{N+1} \tilde{T}_{3,k} = O\left((\tau - \tau_{cap})\rho v_{cv} g \frac{r_{cv}^2}{X_{cv}}\right) = O(\rho g r_{cv}^2), \tag{B17}$$

where we have additionally assumed that $\hat{\Phi} = O(gr_{cv})$ over $S_{cv,cir}$, and $\hat{\Phi} = O(gl_{cv})$ over $S_{cv,end}$.

B.6. *Examining term* $\sum_{k=1}^{N+1} \tilde{T}_{4,k}$

This term is a contributor to the work that the interfaces outside the CV do on the material inside the CV. Using (3.16) and (3.20), this term is given by

$$\sum_{k=1}^{N+1} \tilde{T}_{4,k} = -\frac{1}{A_{cv}} \sum_{k=1}^{N+1} \int_{\widetilde{\Delta t}_k} \int_{S_{cv}} \sum_{i<j} \sigma_{ij}\delta_{S,ij}\boldsymbol{n}_{S,ij}\boldsymbol{n}_{S,ij} : \boldsymbol{v}\boldsymbol{n}_{cv}\, \mathrm{d}S\, \mathrm{d}t. \tag{B18}$$

As the integral contains the surface delta function $\delta_{S,ij}$, like $\tilde{T}_{1,k}$, only four component surfaces of S_{cv} give non-zero contributions to the integral: namely, $S_{cv,top}$, $S_{cv,bl}$, $S_{cv,br}$ and $S_{cv,end}$. We evaluate $\boldsymbol{n}_{S,ij}\boldsymbol{n}_{S,ij} : \tilde{\boldsymbol{v}}\boldsymbol{n}_{cv}$ on each of these surfaces.

On $S_{cv,top}$, $\boldsymbol{n}_{cv} \cdot \boldsymbol{n}_{S,ij} = 0$ as here the fluid interface is perfectly flat and normal to the CV boundary (as discussed in § 3.1), so this surface makes no contribution to (B18). For $S_{cv,bl}$ and $S_{cv,br}$, the interfaces associated with these surface areas have $\boldsymbol{v} = 0$ (the solid velocity) at the CV circumference, so these surfaces also make no contribution to $\tilde{T}_{4,k}$. Finally, over $S_{cv,end}$, at distances from the TPCL that are much larger than $O(h_{rough})$, $\boldsymbol{n}_{S,ij} \cdot \boldsymbol{n}_{cv} = 0$ because, as over $S_{cv,top}$, here the fluid interface is flat and normal to the CV boundary. However, at distances from the TPCL on $S_{cv,end}$ that are of $O(h_{rough})$, $\boldsymbol{n}_{S,ij} \cdot \boldsymbol{n}_{cv}$ is not zero as in this region the interface has curvature of $O(1/h_{rough})$, as described in § 3.1. Further, within this region, the fluid velocity is $\tilde{\boldsymbol{v}} = O(v_{cv})$ as the TPCL may be advancing

over the solid here during these equilibrium stages. Hence there is a contribution to the integral in (B18) from the inner part of $S_{cv,end}$ only, giving overall

$$\sum_{k=1}^{N+1} \tilde{T}_{4,k} = O\left((\tau - \tau_{cap})\sigma v_{cv} \frac{h_{rough}}{X_{cv} l_{cv}}\right) = O\left(\sigma \frac{h_{rough}}{l_{cv}}\right), \tag{B19}$$

where, as per (3.6), a term involving the factor τ_{cap}/τ has been neglected.

B.7. *Examining term* $\sum_{k=1}^{N+1} \tilde{T}_{5,k}$

This term represents the work that the material stresses T_M are doing on the material inside the CV. Using (3.17) and (3.20), this term is defined as

$$\sum_{k=1}^{N+1} \tilde{T}_{5,k} = \frac{1}{A_{cv}} \sum_{k=1}^{N+1} \int_{\widetilde{\Delta t}_k} \int_{S_{cv}} T_M : \boldsymbol{v}\boldsymbol{n}_{cv} \, \mathrm{d}S \, \mathrm{d}t. \tag{B20}$$

Noting that within the solid $\boldsymbol{v} = \boldsymbol{0}$ (as discussed § 3.2), and applying the fluid Newtonian stress equation (3.4), this term can be written as

$$\begin{aligned}\sum_{k=1}^{N+1} \tilde{T}_{5,k} = &-\frac{1}{A_{cv}} \sum_{k=1}^{N+1} \int_{\widetilde{\Delta t}_k} \int_{S_{cv,fluid}} \tilde{p}\tilde{\boldsymbol{v}} \cdot \boldsymbol{n}_{cv} \, \mathrm{d}S \, \mathrm{d}t \\ &+ \frac{1}{A_{cv}} \sum_{k=1}^{N+1} \int_{\widetilde{\Delta t}_k} \int_{S_{cv,fluid}} \mu[\widetilde{\nabla}\boldsymbol{v} + (\widetilde{\nabla}\boldsymbol{v})^{\mathrm{T}}] : \tilde{\boldsymbol{v}}\boldsymbol{n}_{cv} \, \mathrm{d}S \, \mathrm{d}t,\end{aligned} \tag{B21}$$

where we have used the identity $\boldsymbol{I} : \tilde{\boldsymbol{v}}\boldsymbol{n}_{cv} = \tilde{\boldsymbol{v}} \cdot \boldsymbol{n}_{cv}$, and $S_{cv,fluid}$ represents the surface of the CV within the fluid phase. Equilibrium stage fluid properties $\tilde{p}$ and $\widetilde{\nabla}\boldsymbol{v}$ are relevant during these time intervals and are substituted from the steady-state order of magnitude expressions (3.9) and (3.7), respectively, as discussed in § 3.2, giving

$$\begin{aligned}\sum_{k=1}^{N+1} \tilde{T}_{5,k} = &-\frac{\tau - \tau_{cap}}{X_{cv} l_{cv}} \\ &\times \int_{S_{cv,fluid}} \left[O\left(\rho v_{cv}^2 + \frac{\mu v_{cv}}{\max(r, h_{mol})} + \frac{\sigma}{h_{surround}} + \rho g r_{cv}\right) + p_0\right] \tilde{\boldsymbol{v}} \cdot \boldsymbol{n}_{cv} \, \mathrm{d}S \\ &+ \frac{\tau - \tau_{cap}}{X_{cv} l_{cv}} \int_{S_{cv,fluid}} O\left(\frac{\mu v_{cv}}{\max(r, h_{mol})}\right) : \tilde{\boldsymbol{v}}\boldsymbol{n}_{cv} \, \mathrm{d}S.\end{aligned} \tag{B22}$$

For the term involving the reference pressure p_0, as this is constant at any given time, it can come out of the integral, leaving $\tilde{\boldsymbol{v}} \cdot \boldsymbol{n}_{cv}$, which is zero when integrated over $S_{cv,fluid}$ as the fluid is incompressible (using Gauss' theorem). Hence this reference pressure term does not contribute to $\tilde{T}_{5,k}$. For the remainder, we gather like terms and evaluate in an order of magnitude sense over the circumference and ends of the CV that are within the fluid region:

$$\sum_{k=1}^{N+1} \tilde{T}_{5,k} = O\left\{\left(1 - \frac{\tau_{cap}}{\tau}\right) \frac{1}{l_{cv}} \left[\int_{S_{cv,cir}} \left(\rho v_{cv}^2 + \frac{\mu v_{cv}}{\max(r, h_{mol})} + \frac{\sigma}{h_{surround}} + \rho g r_{cv}\right) \mathrm{d}S\right.\right.$$

$$+\int_{S_{cv,end}}\left(\rho v_{cv}^2+\frac{\mu v_{cv}}{\max(r,h_{mol})}+\frac{\sigma}{h_{surround}}+\rho g r_{cv}\right)\mathrm{d}S\Bigg]\Bigg\}$$

$$=O\left\{\left(1-\frac{\tau_{cap}}{\tau}\right)\frac{1}{l_{cv}}\left[\left(\rho v_{cv}^2+\frac{\mu v_{cv}}{r_{cv}}+\frac{\sigma}{h_{surround}}+\rho g r_{cv}\right)r_{cv}l_{cv}\right.\right.$$

$$\left.\left.+\rho v_{cv}^2 r_{cv}^2+\rho g r_{cv}^3+\int_0^{h_{mol}}\frac{\mu v_{cv}}{h_{mol}}\,r\,\mathrm{d}r+\int_{h_{mol}}^{r_{cv}}\frac{\mu v_{cv}}{r}\,r\,\mathrm{d}r+\frac{\sigma r_{cv}^2}{h_{surround}}\right]\right\}$$

$$=O(\rho v_{cv}^2 r_{cv})+O(\mu v_{cv})+O\left(\frac{\sigma r_{cv}}{h_{surround}}\right)+O(\rho g r_{cv}^2), \tag{B23}$$

where for the last line we have used $O(r_{cv})=O(l_{cv})$ and employed (3.1) and (3.6) to neglect comparatively small terms.

B.8. *Examining term* $\sum_{k=1}^{N+1}\tilde{T}_{6,k}$

This final term represents the rate of dissipation occurring within the CV during the equilibrium periods, and is evaluated in a very similar manner to $\tilde{T}_{5,k}$. Using (3.18) and (3.20), this term is defined as

$$\sum_{k=1}^{N+1}\tilde{T}_{6,k}=-\frac{1}{A_{cv}}\sum_{k=1}^{N+1}\int_{\widetilde{\Delta t}_k}\int_{V_{cv}}T_M:\boldsymbol{\nabla v}\boldsymbol{n}_{cv}\,\mathrm{d}V\,\mathrm{d}t. \tag{B24}$$

Noting again that within the solid $\boldsymbol{v}=\boldsymbol{0}$, and applying the fluid Newtonian stress equation (3.4), we find

$$\sum_{k=1}^{N+1}\tilde{T}_{6,k}=\frac{1}{A_{cv}}\sum_{k=1}^{N+1}\int_{\widetilde{\Delta t}_k}\int_{V_{cv,fluid}}\tilde{p}\boldsymbol{I}:\widetilde{\boldsymbol{\nabla}}\boldsymbol{v}\,\mathrm{d}V\,\mathrm{d}t$$

$$-\frac{1}{A_{cv}}\sum_{k=1}^{N+1}\int_{\widetilde{\Delta t}_k}\int_{V_{cv,fluid}}\mu[\widetilde{\boldsymbol{\nabla}}\boldsymbol{v}+(\widetilde{\boldsymbol{\nabla}}\boldsymbol{v})^{\mathrm{T}}]:\widetilde{\boldsymbol{\nabla}}\boldsymbol{v}\,\mathrm{d}V\,\mathrm{d}t. \tag{B25}$$

For the pressure term, we use $\boldsymbol{I}:\widetilde{\boldsymbol{\nabla}}\boldsymbol{v}=\boldsymbol{\nabla}\cdot\tilde{\boldsymbol{v}}=0$ as the fluid is incompressible, removing this entire integral. Substituting the equilibrium stage fluid velocity gradient from (3.7) into the remaining dissipation integral and evaluating in an order of magnitude sense leads to

$$\sum_{k=1}^{N+1}\tilde{T}_{6,k}=O\left(\frac{\mu(\tau-\tau_{cap})}{A_{cv}}\int_{V_{cv,fluid}}\frac{v_{cv}^2}{[\max(r,h_{mol})]^2}\,\mathrm{d}V\right)$$

$$=O\left[\mu v_{cv}\left(1-\frac{\tau_{cap}}{\tau}\right)\left(\int_0^{h_{mol}}\frac{r}{h_{mol}^2}\,\mathrm{d}r+\int_{h_{mol}}^{r_{cv}}\frac{1}{r}\,\mathrm{d}r\right)\right]$$

$$=O\left[\mu v_{cv}\ln\left(\frac{r_{cv}}{h_{mol}}\right)\right], \tag{B26}$$

where again relatively small terms have been neglected via (3.1) and (3.6).

Appendix C. Dissipation event order of magnitude energy analysis

As discussed in the main text, the objective of this appendix is to quantify in an order of magnitude sense what energy terms are significant during the dissipation events so that we can determine the ultimate destination for the specific surface energy $\widehat{\Delta\sigma}$ that is liberated from the dissipation events.

Summing the individual dissipation event energy balances expressed by (3.24) over all N dissipation events and substituting the order of magnitude of $\sum_{k=1}^{N}\hat{T}_{0,k}$ from (B6) gives

$$O(\rho v_{cv}^2\, h_{rough}) + O(\rho g\, h_{rough}^2) + \widehat{\Delta\sigma} = \sum_{k=1}^{N}\hat{T}_{0,k} = \sum_{i=1}^{6}\sum_{k=1}^{N}\hat{T}_{i,k}. \tag{C1}$$

We now examine each of the six $\sum_{k=1}^{N}\hat{T}_{i,k}$ terms on the right-hand side of this equation.

For $\hat{T}_{1,k}$, as for the equilibrium analysis $\boldsymbol{n}_{cv}\cdot\boldsymbol{v}_{cv}$ on $S_{cv,end}$, so the only contribution to this term comes from $S_{cv,cir}$. However, on the circumference of the CV, the interface is not affected by the dissipation event (as it is $O(r_{cv})$ away from $\boldsymbol{x}_{cap}$) so that the value of the surface integral is independent of whether the time is within an equilibrium or dissipation stage. Noting then that $\sum_{k=1}^{N}\int_{\widehat{\Delta t}_k} dt = \tau_{cap}$ and $\sum_{k=1}^{N+1}\int_{\widetilde{\Delta t}_k} \mathrm{d}t = \tau - \tau_{cap}$, the first dissipation term can be written as

$$\begin{aligned}\sum_{k=1}^{N}\hat{T}_{1,k} &= \frac{1}{A_{cv}}\sum_{k=1}^{N}\int_{\widehat{\Delta t}_k}\int_{S_{cv}}\sum_{i<j}\sigma_{ij}\delta_{S,ij}\boldsymbol{n}_{cv}\cdot\boldsymbol{v}_{cv}\,\mathrm{d}S\,\mathrm{d}t\\ &= \frac{\tau_{cap}}{\tau-\tau_{cap}}\sum_{k=1}^{N+1}\tilde{T}_{1,k} = O\left(\frac{\tau_{cap}}{\tau}\sum_{k=1}^{N+1}\tilde{T}_{1,k}\right),\end{aligned} \tag{C2}$$

where (3.6) has been utilised.

The second term on the right-hand side of (C1) is concerned with movement of kinetic energy through the CV boundary during the dissipation periods. Using the stationary solid model, this term is

$$\sum_{k=1}^{N}\hat{T}_{2,k} = \frac{1}{A_{cv}}\sum_{k=1}^{N}\int_{\widehat{\Delta t}_k}\int_{S_{cv,fluid}}\boldsymbol{n}_{cv}\cdot\frac{1}{2}\,\rho\,|\hat{\boldsymbol{v}}|^2(\boldsymbol{v}_{cv}-\hat{\boldsymbol{v}})\,\mathrm{d}S\,\mathrm{d}t. \tag{C3}$$

By recognising the separation of velocities $v_{cv} \ll v_{cap}$ when using (3.32) in the above, for order of magnitude purposes, products of v_{cv} and v_{cap} can be ignored, and the above term written as a contribution from the continuous and dissipation interface movements as

$$\begin{aligned}\sum_{k=1}^{N}\hat{T}_{2,k} &= O\left(\frac{\tau_{cap}}{\tau-\tau_{cap}}\sum_{k=1}^{N+1}\tilde{T}_{2,k}\right) + O\left(\frac{\rho v_{cap}^3\tau_{cap}\,h_{rough}^3}{A_{cv}l_{cv}}\right)\\ &= O\left(\frac{\tau_{cap}}{\tau}\sum_{k=1}^{N+1}\tilde{T}_{2,k}\right) + O\left(\frac{\rho v_{cap}^2\,h_{rough}^2}{l_{cv}}\right).\end{aligned} \tag{C4}$$

In evaluating the dissipation event term on the first line of this equation (the second on the right-hand side), consistent with the dissipation fluid model of (3.32), $\hat{\boldsymbol{v}}$ is significant only within an area of $O(h_{rough}^2)$ on each end of the CV, and as the dissipation events are evenly distributed over the length l_{cv} of the CV, only a proportion $O(h_{rough}/l_{cv})$ of the dissipation events contribute to this surface integral. Further, from (3.6) we have used $\tau_{cap} v_{cap} = O(l_{cv} X_{cv}/h_{rough})$.

The third term on the right-hand side of (C1) represents transport of gravitational potential energy over the CV boundary and is evaluated in a very similar fashion to the second term. Recognising as previously that energy transport due to specific dissipation movements only occurs over the central $O(h_{rough}^2)$ area of $S_{cv,end}$, and that during these events $\hat{\Phi} = O(g h_{rough})$, this term can be evaluated as

$$\begin{aligned}\sum_{k=1}^{N} \hat{T}_{3,k} &= \frac{1}{A_{cv}} \sum_{k=1}^{N} \int_{\widehat{\Delta t}_k} \int_{S_{cv,fluid}} \boldsymbol{n}_{cv} \cdot \rho\, \hat{\Phi} (\boldsymbol{v}_{cv} - \hat{\boldsymbol{v}}) \,\mathrm{d}S \,\mathrm{d}t \\ &= O\left(\frac{\tau_{cap}}{\tau} \sum_{k=1}^{N+1} \tilde{T}_{3,k}\right) + O\left(\frac{\rho g\, h_{rough}^3}{l_{cv}}\right),\end{aligned} \tag{C5}$$

where assumptions consistent with those used for (C4) have been employed, and the first and second terms on the right-hand side of the second line of this equation represent contributions from the continuous and dissipation velocities occurring during the dissipation periods, respectively.

Term $\sum_{k=1}^{N} \hat{T}_{4,k}$, like $\sum_{k=1}^{N} \hat{T}_{1,k}$, is concerned with interfacial behaviour at the CV boundary. Recognising that only the interface between the two fluids can experience a non-zero velocity, and that dissipation interfacial movements are again confined to an area of $O(h_{rough}^2)$ on $S_{cv,end}$, this term can be written as

$$\begin{aligned}\sum_{k=1}^{N} \hat{T}_{4,k} &= -\frac{1}{A_{cv}} \sum_{k=1}^{N} \int_{\widehat{\Delta t}_k} \int_{S_{cv,fluid}} \sigma_{12} \delta_{S,12} \boldsymbol{n}_{S,12} \boldsymbol{n}_{S,12} : \hat{\boldsymbol{v}} \boldsymbol{n}_{cv} \,\mathrm{d}S \,\mathrm{d}t \\ &= O\left(\frac{\tau_{cap}}{\tau} \sum_{k=1}^{N+1} \tilde{T}_{4,k}\right) + O\left(\sigma\, \frac{h_{rough}}{l_{cv}}\right),\end{aligned} \tag{C6}$$

where $\tau_{cap} v_{cap}$ has again been evaluated using (3.6).

The final two terms from the right-hand side of (C1) are concerned with material stresses, specifically representing the boundary work and internal viscous dissipation occurring on and within the CV, respectively. As per previously in the absence of solid velocities, these terms only have contributions from the fluid regions. For the boundary work term, we substitute the Newtonian stress equation (3.4) and dissipation period velocity, velocity gradient and pressure expressions of (3.32), (3.33) and (3.34),

respectively, into (3.17) applied over the dissipation periods, giving

$$\sum_{k=1}^{N}\hat{T}_{5,k} = -\frac{1}{A_{cv}}\sum_{k=1}^{N}\int_{\widehat{\Delta t}_k}\int_{S_{cv,fluid}}\hat{p}\hat{\boldsymbol{v}}\cdot\boldsymbol{n}_{cv}\,\mathrm{d}S\,\mathrm{d}t + \frac{1}{A_{cv}}\sum_{k=1}^{N}\int_{\widehat{\Delta t}_k}\int_{S_{cv,fluid}}\mu[\widehat{\nabla\boldsymbol{v}}+(\widehat{\nabla\boldsymbol{v}})^{\mathrm{T}}]:\hat{\boldsymbol{v}}\boldsymbol{n}_{cv}\,\mathrm{d}S\,\mathrm{d}t$$
$$= O\left(\frac{\tau_{cap}}{\tau-\tau_{cap}}\sum_{k=1}^{N+1}\tilde{T}_{5,k}\right) + O\left(\frac{v_{cap}\tau_{cap}\,h_{rough}}{A_{cv}l_{cv}} \times \int_{S_{cv,end},r<h_{rough}}\left[\frac{\mu v_{cap}}{\max(r,h_{mol})}+\rho v_{cap}^2+\frac{\sigma}{h_{rough}}\right]\mathrm{d}S\right). \tag{C7}$$

The final integral in this equation is taken over the ends of the CV that are within $O(h_{rough})$ of its centreline, with r representing the distance to the centreline. Evaluating this integral leads to

$$\sum_{k=1}^{N}\hat{T}_{5,k} = O\left(\frac{\tau_{cap}}{\tau}\sum_{k=1}^{N+1}\tilde{T}_{5,k}\right) + O\left(\rho v_{cap}^2\frac{h_{rough}^2}{l_{cv}}\right) + O\left(\mu v_{cap}\frac{h_{rough}}{l_{cv}}\right) + O\left(\sigma\frac{h_{rough}}{l_{cv}}\right). \tag{C8}$$

The viscous dissipation term $\sum_{k=1}^{N}\hat{T}_{6,k}$ is evaluated similarly. Noting that velocities within the solid are zero, and that the fluid is incompressible, as for the corresponding equilibrium term analysis, there is no contribution from the pressure term $\hat{p}$, and the dissipation velocity gradient can be integrated over a region of volume $O(h_{rough}^3)$ within the fluid, giving

$$\sum_{k=1}^{N}\hat{T}_{6,k} = -\frac{1}{A_{cv}}\sum_{k=1}^{N}\int_{\widehat{\Delta t}_k}\int_{V_{cv,fluid}}\mu[\widehat{\nabla\boldsymbol{v}}+(\widehat{\nabla\boldsymbol{v}})^{\mathrm{T}}]:\widehat{\nabla\boldsymbol{v}}\,\mathrm{d}V\,\mathrm{d}t$$
$$= O\left(\frac{\tau_{cap}}{\tau}\sum_{k=1}^{N+1}\tilde{T}_{6,k}\right) + O\left(\mu v_{cap}\ln\left(\frac{h_{rough}}{h_{mol}}\right)\right). \tag{C9}$$

Equation (3.35) in the main text results from substituting (C2), (C4), (C5), (C6), (C8) and (C9) into (C1).

References

Amirfazli, A. & Neumann, A.W. 2004 Status of the three-phase line tension: a review. *Adv. Colloid Interface Sci.* **110** (3), 121–141.

Aris, R. 1962 *Vectors, Tensors, and the Basic Equations of Fluid Mechanics*. Dover.

Batchelor, G.K. 1967 *An Introduction to Fluid Dynamics*. Cambridge University Press.

Bico, J., Marzolin, C. & Quéré, D. 1999 Pearl drops. *Europhys. Lett.* **47** (2), 220–226.

Bico, J., Thiele, U. & Quéré, D. 2002 Wetting of textured surfaces. *Colloids Surf.* **206**, 41–46.

Bird, R.B., Stewart, W.E. & Lightfoot, E.N. 2002 *Transport Phenomena*, 2nd edn. John Wiley and Sons.

BLAKE, T.D. & HAYNES, J.M. 1969 Kinetics of liquid/liquid displacement. *J. Colloid Interface Sci.* **30** (3), 421–423.

BORUVKA, L. & NEUMANN, A.W. 1977 Generalization of the classical theory of capillarity. *J. Chem. Phys.* **66** (12), 5464–5476.

BRACKBILL, J.U., KOTHE, D.B. & ZEMACH, C. 1992 A continuum method for modelling surface tension. *J. Comput. Phys.* **100**, 335–354.

BRANDON, S., HAIMOVICH, N., YEGER, E. & MARMUR, A. 2003 Partial wetting of chemically patterned surfaces: the effect of drop size. *J. Colloid Interface Sci.* **263**, 237–243.

BROCHARD-WYART, F. & DE GENNES, P.G. 1992 Dynamics of partial wetting. *Adv. Colloid Interface Sci.* **39**, 1–11.

BUTT, H.-J., GAO, N., PAPADOPOULOS, P., STEFFEN, W., KAPPL, M. & BERGER, R. 2017 Energy dissipation of moving drops on superhydrophobic and superoleophobic surfaces. *Langmuir* **33** (1), 107–116.

BUTT, H.-J., *et al.* 2022 Contact angle hysteresis. *Curr. Opin. Colloid Interface Sci.* **59**, 101574.

CALLIES, M. & QUÉRÉ, D. 2005 On water repellency. *Soft Matter* **1**, 55–61.

CASSIE, A.B.D. & BAXTER, S. 1944 Wettability of porous surfaces. *Trans. Faraday Soc.* **40**, 546–551.

CHOI, W., TUTEJA, A., MABRY, J.M., COHEN, R.E. & MCKINLEY, G.H. 2009 A modified Cassie–Baxter relationship to explain contact angle hysteresis and anisotropy on non-wetting textured surfaces. *J. Colloid Interface Sci.* **339** (1), 208–216.

COX, R.G. 1983 The spreading of a liquid on a rough solid surface. *J. Fluid Mech.* **131**, 1–26.

DAHLER, J.S. & SCRIVEN, L.E. 1961 Angular momentum of continua. *Nature* **192**, 36–37.

DE GENNES, P.G. 1985 Wetting: statics and dynamics. *Rev. Mod. Phys.* **57** (3), 827–863.

DELMAS, M., MONTHIOUX, M. & ONDARÇUHU, T. 2011 Contact angle hysteresis at the nanometer scale. *Phys. Rev. Lett.* **106** (13), 136102.

DORRER, C. & RÜHE, J. 2008 Drops on microstructured surfaces coated with hydrophilic polymers: Wenzel's model and beyond. *Langmuir* **24** (5), 1959–1964.

ERAL, H.B., 'T MANNETJE, D.J.C.M. & OH, J.M. 2013 Contact angle hysteresis: a review of fundamentals and applications. *Colloid Polym. Sci.* **291** (2), 247–260.

ERBIL, H.Y. 2021 Dependency of contact angles on three-phase contact line: a review. *Colloids Interfaces* **5** (1), 8.

ERBIL, H.Y. & CANSOY, C.E. 2009 Range of applicability of the Wenzel and Cassie–Baxter equations for superhydrophobic surfaces. *Langmuir* **25** (24), 14135–14145.

EXTRAND, C.W. 1998 A thermodynamic model for contact angle hysteresis. *J. Colloid Interface Sci.* **207** (1), 11–19.

EXTRAND, C.W. 2002 Model for contact angles and hysteresis on rough and ultraphobic surfaces. *Langmuir* **18**, 7991–7999.

EXTRAND, C.W. 2003 Contact angles and hysteresis on surfaces with chemically heterogeneous islands. *Langmuir* **19** (9), 3793–3796.

FENG, L., LI, S., LI, Y., LI, H., ZHANG, L., ZHAI, J., SONG, Y., LIU, B., JIANG, L. & ZHU, D. 2002 Super-hydrophobic surfaces: from natural to artificial. *Adv. Mater.* **14**, 1857–1860.

FENG, L., MAI, Z.Z.Z., MA, Y., LIU, B., JIANG, L. & ZHU, D. 2004 A super-hydrophobic and super-oleophilic coating mesh film for the separation of oil and water. *Angew. Chem. Intl Ed.* **43**, 2012–2014.

FETZER, R. & RALSTON, J. 2011 Exploring defect height and angle on asymmetric contact line pinning. *J. Phys. Chem.* C **115** (30), 14907–14913.

FORSBERG, P.S.H., PRIEST, C., BRINKMANN, M., SEDEV, R. & RALSTON, J. 2010 Contact line pinning on microstructured surfaces for liquids in the Wenzel state. *Langmuir* **26** (2), 860–865.

GAO, L. & MCCARTHY, T.J. 2007*a* How Wenzel and Cassie were wrong. *Langmuir* **23** (7), 3762–3765.

GAO, L. & MCCARTHY, T.J. 2007*b* Reply to 'Comment on how Wenzel and Cassie were wrong by Gao and McCarthy'. *Langmuir* **23** (26), 13243–13243.

GAYDOS, J. & NEUMANN, A.W. 1987 The dependence of contact angles on drop size and line tension. *J. Colloid Interface Sci.* **120** (1), 76–86.

HARVIE, D.J.E., ZHANG, X., STADLER, B.M. & DUCKER, W. 2008 Contact angle hysteresis on sparsely structured surfaces. In *82nd ACS Colloid and Surface Science Symposium*. Raleigh, NC, USA, presentation.

HUANG, Z. 2020 New equations of wetting. *Phil. Mag. Lett.* **100** (4), 181–188.

HUH, C. & SCRIVEN, L.E. 1971 Hydrodynamic model of steady movement of a solid/liquid/fluid contact line. *J. Colloid Interface Sci.* **35** (1), 85–101.

ILIEV, S., PESHEVA, N. & ILIEV, P. 2023 Contact angle hysteresis on random self-affine rough surfaces in Wenzel's wetting regime: numerical study. *Phys. Rev.* E **107** (2), 024802.

JAMES, A.J. & LOWENGRUB, J. 2004 A surfactant-conserving volume-of-fluid method for interfacial flows with insoluble surfactant. *J. Comput. Phys.* **201**, 685–722.

JIANG, Y., XU, W., SARSHAR, M.A. & CHOI, C.-H. 2019 Generalized models for advancing and receding contact angles of Fakir droplets on pillared and pored surfaces. *J. Colloid Interface Sci.* **552**, 359–371.

JOANNY, J.F. & DE GENNES, P.G. 1984 A model for contact angle hysteresis. *J. Phys. Chem.* **81** (1), 552–562.

JOHNSON, R.E. JR. & DETTRE, R.H. 1964 I: Study of an idealized rough surface. In *Contact Angle, Wettability, and Adhesion*, Advances in Chemistry, vol. 43, pp. 112–135. American Chemical Society.

KARIM, A.M. 2022 A review of physics of moving contact line dynamics models and its applications in interfacial science. *J. Appl. Phys.* **132** (8), 080701.

KREYSZIG, E. 2006 *Advanced Engineering Mathematics*, 9th edn. John Wiley and Sons.

KUIKEN, G.D.C. 1995 The symmetry of the stress tensor. *Ind. Engng Chem. Res.* **34** (10), 3568–3572.

KUMAR, P. & HARVIE, D.J.E. 2024 Energy dissipation during Wenzel wetting via roughness scale interface dynamics. *Langmuir*, submitted.

KUMAR, P., MULVANEY, P. & HARVIE, D.J.E. 2024 Energy dissipation during homogeneous wetting of surfaces with randomly and periodically distributed cylindrical pillars. *J. Colloid Interface Sci.* **659**, 105–118.

LAFAURIE, B., NARDONE, C., SCARDOVELLI, R., ZALESKI, S. & ZANETTI, G. 1994 Modelling merging and fragmentation in multiphase flows with SURFER. *J. Comput. Phys.* **113**, 134–147.

LI, D., XUE, Y., LV, P., HUANG, S., LIN, H. & DUAN, H. 2016 Receding dynamics of contact lines and size-dependent adhesion on microstructured hydrophobic surfaces. *Soft Matter* **12** (18), 4257–4265.

LI, K., JU, J., XUE, Z., MA, J., FENG, L., GAO, S. & JIANG, L. 2013 Structured cone arrays for continuous and effective collection of micron-sized oil droplets from water. *Nat. Commun.* **4**, 2276.

MAKKONEN, L. 2017 A thermodynamic model of contact angle hysteresis. *J. Chem. Phys.* **147** (6), 064703.

MARMUR, A. 1997 Line tension and the intrinsic contact angle in solid–liquid–fluid systems. *J. Colloid Interface Sci.* **186**, 462–466.

MARMUR, A. 2006 Soft contact: measurement and interpretation of contact angles. *Soft Matter* **2**, 12–17.

MARMUR, A. 2022 The contact angle hysteresis puzzle. *Colloids Interfaces* **6** (3), 39.

MCHALE, G. 2007 Cassie and Wenzel: were they really so wrong? *Langmuir* **23** (15), 8200–8205.

MOFFATT, H.K. 1964 Viscous and resistive eddies near a sharp corner. *J. Fluid Mech.* **18** (1), 1–18.

NOSONOVSKY, M. 2007 On the range of applicability of the Wenzel and Cassie equations. *Langmuir* **23** (19), 9919–9920.

ÖNER, D. & MCCARTHY, T.J. 2000 Ultrahydrophobic surfaces, effects of topography length scales on wettability. *Langmuir* **16**, 7777–7782.

ÖPIK, U. 2000 Contact-angle hysteresis caused by a random distribution of weak heterogeneities on a solid surface. *J. Colloid Interface Sci.* **223** (2), 143–166.

PANCHAGNULA, M.V. & VEDANTAM, S. 2007 Comment on how Wenzel and Cassie were wrong by Gao and McCarthy. *Langmuir* **23** (26), 13242–13242.

PATANKAR, N.A. 2003 On the modelling of hydrophobic contact angles on rough surfaces. *Langmuir* **19**, 1249–1253.

PETROV, P. & PETROV, I. 1992 A combined molecular–hydrodynamic approach to wetting kinetics. *Langmuir* **8** (7), 1762–1767.

POMEAU, Y. & VANNIMENUS, J. 1985 Contact angle on heterogeneous surfaces: weak heterogeneities. *J. Colloid Interface Sci.* **104** (2), 477–488.

POMPE, T., FERY, A. & HERMINGHAUS, S. 1999 Measurement of contact line tension by analysis of the three-phase boundary with nanometer resolution. *J. Adhes. Sci. Technol.* **13** (10), 1155–1164.

PRIEST, C., ALBRECHT, T.W.J., SEDEV, R. & RALSTON, J. 2009 Asymmetric wetting hysteresis on hydrophobic microstructured surfaces. *Langmuir* **25** (10), 5655–5660.

PRIEST, C., SEDEV, R. & RALSTON, J. 2007 Asymmetric wetting hysteresis on chemical defects. *Phys. Rev. Lett.* **99** (2), 026103.

PRIEST, C., SEDEV, R. & RALSTON, J. 2013 A quantitative experimental study of wetting hysteresis on discrete and continuous chemical heterogeneities. *Colloid Polym. Sci.* **291** (2), 271–277.

RAJ, R., ENRIGHT, R., ZHU, Y., ADERA, S. & WANG, E.N. 2012 Unified model for contact angle hysteresis on heterogeneous and superhydrophobic surfaces. *Langmuir* **28** (45), 15777–15788.

RAMIASA, M., RALSTON, J., FETZER, R., SEDEV, R., FOPP-SPORI, D.M., MORHARD, C., PACHOLSKI, C. & SPATZ, J.P. 2013 Contact line motion on nanorough surfaces: a thermally activated process. *J. Am. Chem. Soc.* **135** (19), 7159–7171.

REYSSAT, M. & QUÉRÉ, D. 2009 Contact angle hysteresis generated by strong dilute defects. *J. Phys. Chem.* B **113** (12), 3906–3909.

ROBBINS, M.O. & JOANNY, J.F. 1987 Contact angle hysteresis on random surfaces. *Europhys. Lett.* **3** (6), 729.

SCHELLENBERGER, F., ENCINAS, N., VOLLMER, D. & BUTT, H.-J. 2016 How water advances on superhydrophobic surfaces. *Phys. Rev. Lett.* **116** (9), 096101.

SHARDT, N. & ELLIOTT, J.A.W. 2020 Gibbsian thermodynamics of Wenzel wetting (Was Wenzel wrong? Revisited). *Langmuir* **36** (1), 435–446.

SONG, Q., LIU, K., SUN, W., JIAO, Y., WANG, Z., LIU, X. & YE, J. 2022 Contact angle hysteresis and lateral adhesion strength on random rough surfaces. *Phys. Fluids* **34** (8), 082015.

SUN, T.L., FENG, L., GAO, X.F. & JIANG, L. 2005 Bioinspired surfaces with special wettability. *Acc. Chem. Res.* **38**, 644–652.

VOINOV, O.V. 1976 Hydrodynamics of wetting. *Izv. Akad. Nauk SSSR* **5**, 76–84.

WENZEL, R.N. 1936 Resistance of solid surfaces to wetting by water. *Ind. Engng Chem.* **28** (8), 988–994.

WU, Y., SUGIMURA, H., INOUE, Y. & TAKAI, O. 2002 Thin films with nanotextures for transparent and ultra water-repellent coatings produced from trimethylmethoxysilane by microwave plasma CVD. *Chem. Vapor Depos.* **8** (2), 47–49.

XU, X. 2016 Modified Wenzel and Cassie equations for wetting on rough surfaces. *SIAM J. Appl. Math.* **76** (6), 2353–2374.

YUE, P. 2020 Thermodynamically consistent phase-field modelling of contact angle hysteresis. *J. Fluid Mech.* **899**, A15.

ZHU, J. & DAI, X. 2019 A new model for contact angle hysteresis of superhydrophobic surface. *AIP Adv.* **9** (6), 065309.